THESIS

CHARACTERIZATION AND MODELING OF $CdCl_2$ TREATED CdTe/CdS THIN-FILM SOLAR CELLS

Submitted by

Graham Lane Maxwell

Department of Mechanical Engineering

In partial fulfillment of the requirements

For the Degree of Master of Science

Colorado State University

Fort Collins, Colorado

Fall 2010

Master's Committee:

Department Head: Susan P. James

Advisor: Venkatesan Manivannan

W. S. Sampath

James R. Sites

ABSTRACT OF THESIS

CHARACTERIZATION AND MODELING OF $CdCl_2$ TREATED CdTe/CdS THIN-FILM SOLAR CELLS

CdTe photovoltaic technology has the potential to become a leading energy producer in the coming decades. Its physical properties are well suited for photovoltaic energy conversion. A key processing step in the production of high efficiency CdTe/CdS solar cells is a post-CdTe deposition heat treatment with $CdCl_2$, which can improve performance by promoting CdTe rectrystallization, QE response, defect passivation and others. Understanding the effects of the $CdCl_2$ treatment is crucial in order to optimize processing conditions and improve performance. This study investigates the effects of variations of $CdCl_2$ treatment duration on CdTe/CdS solar cells manufactured at Colorado State University. In order to investigate the optimal time of $CdCl_2$ treatment, sample solar cells were tested for microstructural and performance properties. Device microstructure was analyzed using X-ray diffraction (XRD), scanning electron microscopy (SEM), and atomic force microscopy (AFM). Device performance was analyzed using current density-voltage (J-V) measurements, time-resolved photoluminescence (TRPL), quantum efficiency (QE), and laser beam induced current (LBIC) measurements.

Little change in microstructure was observed with extended $CdCl_2$ treatment and is attributed to the high CdTe deposition temperatures used by heat pocket deposition

(HPD). This deposition technique allows for large initial grains to be formed with low lattice strain energy which prevents recrystallization and grain growth that is often seen with other deposition techniques.

The $CdCl_2$ treatment initially improves performance significantly, but it was shown to that extending the $CdCl_2$ treatment can reduce performance. Overall performance was reduced despite an increase in minority carrier lifetime values. The mechanism of reduced performance is suggested to be the formation of a low bandgap CdTe layer resulting from sulfur diffusion from the CdS layer. Sulfur diffusion primarily occurs during the $CdCl_2$ treatment and also leads to thinning of the CdS layer.

Solar cell modeling was employed to investigate possible mechanisms for performance degradation. Modeling was done with AMPS and SCAPS modeling software. Models were created to investigate the effects of minority carrier lifetime, CdS thickness, and a low bandgap CdTe layer. Modeling results showed that the formation of a low bandgap CdTe layer combined with CdS thinning reduces device performance. Further research is needed using a statistically significant number of samples to investigate other possible degradation mechanisms associated with extended $CdCl_2$ treatment.

Graham Lane Maxwell
Department of Mechanical Engineering
Colorado State University
Fort Collins, CO 80523
Fall 2010

ACKNOWLEDGEMENTS

I would first like to thank my advisor, Dr. Manivannan. His continuous help and involvement in my studies was key to my success. I would also like to thank the members of my graduate committee, Dr. Sites and Dr. Sampath. My fellow students, Paul Kobyakov, Jason Kephart, Kevin Walters, and Scott Smith generously contributed their knowledge and helped me greatly. Hsiao Kuo-Jui (Ray) and Russell Geisthardt from the physics photovoltaics laboratory were willing in helping me conduct various measurements. The support of my family from many miles away was amazing and I am blessed to have them. Thanks to the many good friends I have made, who have helped me to remember that you need to have a little fun in life. And to my fiancé, Brittney, I save a special thanks because she allows me to see a piece of God's beauty every day. Lastly, and most of all, I thank God. He makes everything on this earth possible in His time. All the beauty and mystery of science that we study points back to One who created it.

TABLE OF CONTENTS

LIST OF FIGURES

LIST OF TABLES

CHAPTER 1: Introduction

1.1 The Energy Challenge

One of the biggest issues facing our world today is that of energy supply. Readily consumable energy is a vital and indispensible part of the world. Uncertainty abounds about how the world's increasing energy demand will be satisfied. This past century has seen an exponential increase in the demand for energy. The increase in energy use is primarily the result of the rapidly growing world population using an increased amount of technology that requires a greater amount of energy to sustain it. The majority of current energy demand is being satisfied by energy sources that are finite, namely, fossil-based fuels. Energy consumption trends by energy source are shown in Figure 1.1. Energy demand is increasing, but the percentages of energy supplied from the various energy sources have remained fairly constant. Renewable energy production has increased, but the fraction it plays in the total energy supply has not increased significantly. As can be seen in Figure 1.2, renewable energy sources comprise a very small amount of the energy picture. Solar, wind, and other renewable energy sources account for less than one percent of the energy breakdown. With all the publicity and push for renewable energy, the reality is there is a long way to go before it significantly contributes to the world energy supply.

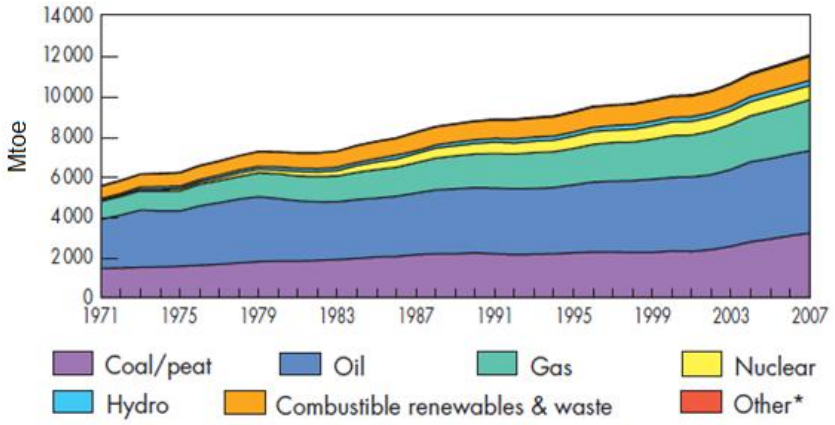

Figure 1.1: World total primary energy supply in Mtoe (million tons of oil equivalent) over the past few decades. Image taken from ref [1].

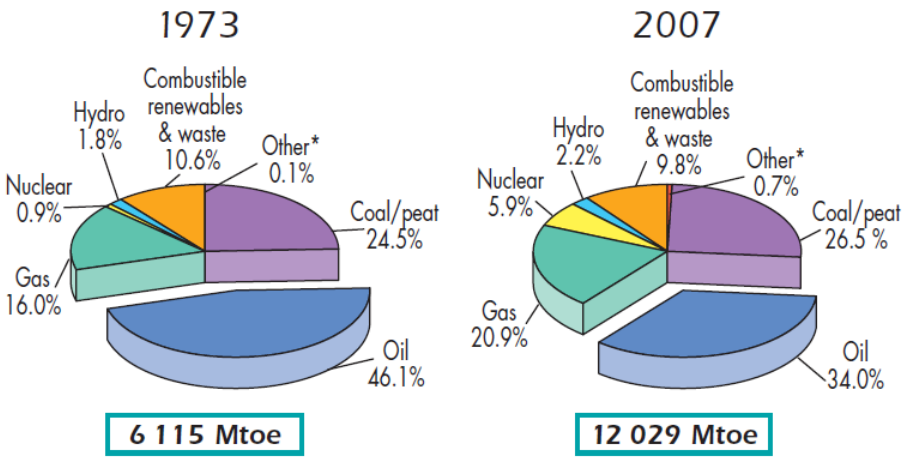

Figure 1.2: Difference in world energy supply by source from 1973 to 2007. "Other" includes renewable energy (solar, wind, etc). Image taken from ref [1].

1.2 Renewable Energy Options

Renewable energy is by definition energy that is derived from sources that are inexhaustible in for the foreseeable future (e.g. the sun is considered a renewable energy source, but will not last indefinitely). It is useful to examine the energy flow of the earth in order to better understand where our energy comes from and where it goes. Figure 1.3

shows the four primary energy sources available on earth. Three of these (atomic energy, solar energy and geothermal) are nuclear based energy sources. The fourth source, planet gravitation and motion, is non-nuclear energy.

Nearly all of the energy sources that are consumed today are descendent from the sun. Our largest energy source consumed today, fossil fuel, is past solar energy converted via photosynthesis, stored in organic matter and over time converted to fossil fuel. Solar radiation accounts for more than 99.9% of the energy present on earth [2]. Figure 1.3 shows that of the solar radiation incident on the earth, over 50% is reflected or absorbed by the atmosphere. The remaining solar energy is either absorbed by the ocean or land and is then converted to various other types of energy (ocean current, wind, evaporation and precipitation). It is interesting to note that compared to solar energy, geothermal energy and gravitational energy contributions are quite small. Even though solar energy is the precursor of many other forms of energy, the term "solar energy" no longer applies once it has been converted to another form of energy. It is clear that there are abundant renewable energy sources available to supply the world's energy needs. The challenge we are facing is developing technologies that can efficiently and inexpensively convert renewable energy sources to useful energy. Figure 1.4 shows how the various forms of renewable energy are converted to useable energy.

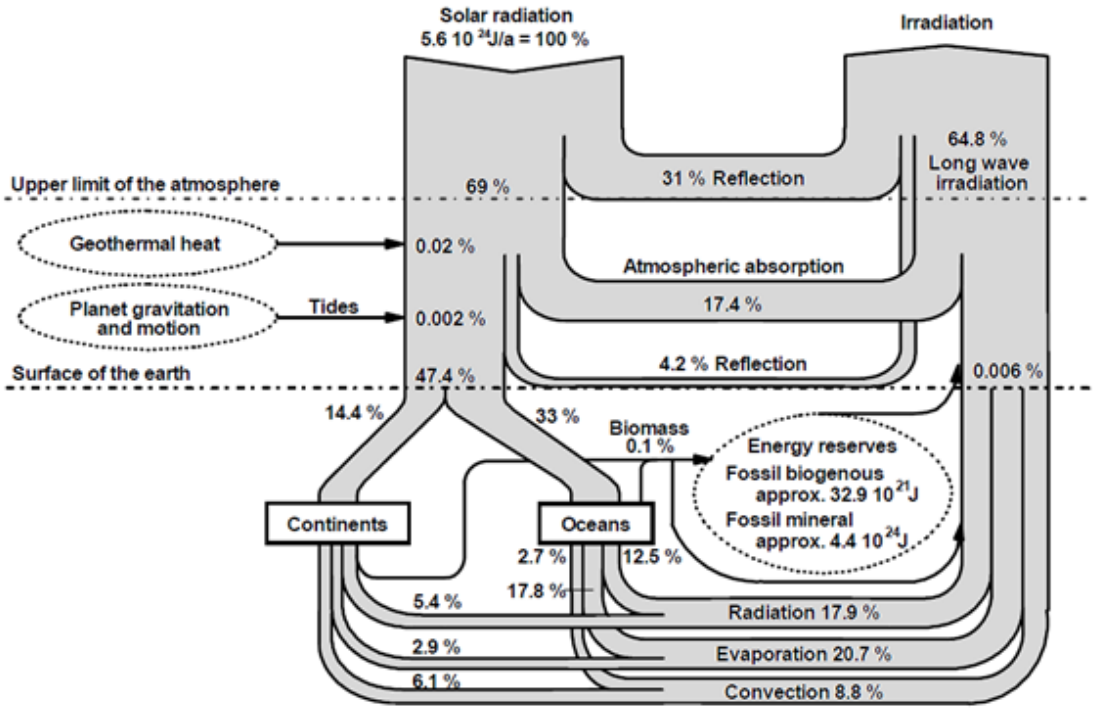

Figure 1.3: Energy balance of the earth. Image taken from ref [2].

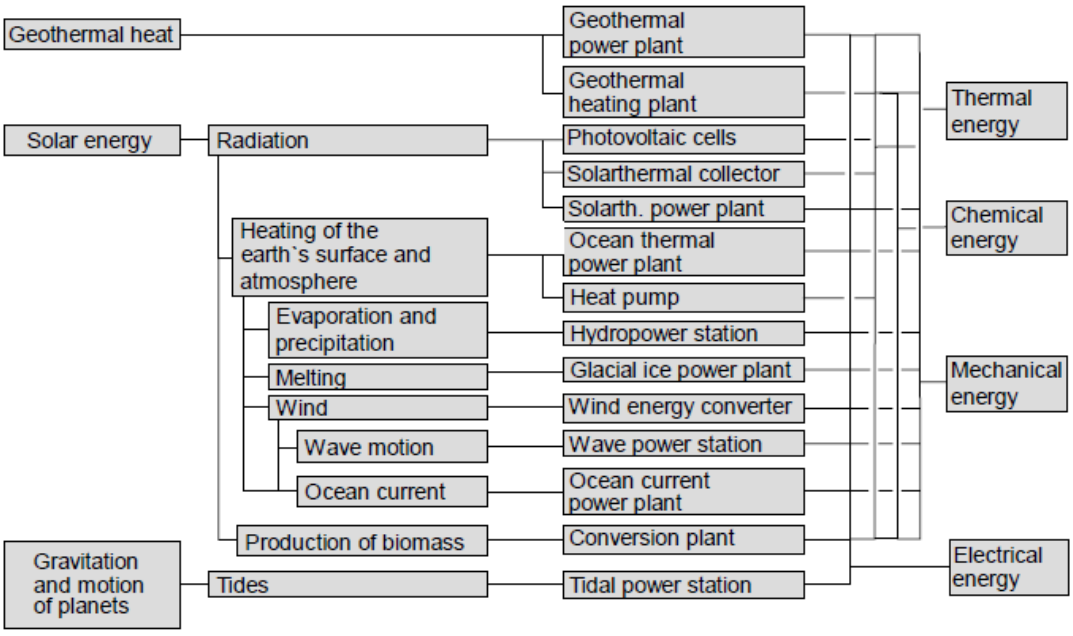

Figure 1.4: Options for converting renewable energy sources into useful energy. Image taken from ref [2].

There most likely will not be a single solution to the energy problem we are facing. There will, however, need to be some renewable energy technologies that are able to carry most of the energy burden currently carried by fossil based fuels. There are several technologies that currently look promising to assume this role. For better or worse, until the cost of renewable energy sources are brought down to a comparable level of current energy sources, progress will be slow. In order to make progress toward an energy future that is primarily dominated by renewables, new technologies must continued to be researched and refined.

One of the leading contenders in the renewable energy scheme is wind energy. The wind has been used by humans for hundreds of years for various tasks. Wind energy is the result of the heating of the earth's surface by solar energy. Of the total solar radiation incident on the earth, approximately 2.5% (1.4×10^{23} joules/year) is converted into wind energy [2]. This translates to a maximum power of 4.4×10^{15} Watts. Due to many factors (wind turbine efficiency, land availability, fluctuating wind speeds, etc) that maximum power can never be reached, but even so, there is still a large amount of wind available to produce energy. Wind energy is not suitable everywhere in the world, as can be seen in Figure 1.5. Wind energy is converted into electricity by wind turbines. Turbine blades convert the wind energy into mechanical energy and then to electrical energy. For large scale power production, many large (~200 ft tall) wind turbines are grouped together in wind farms. Some of the limiting factors of wind energy are the intermittence of power produced, geographic limitations, and high costs.

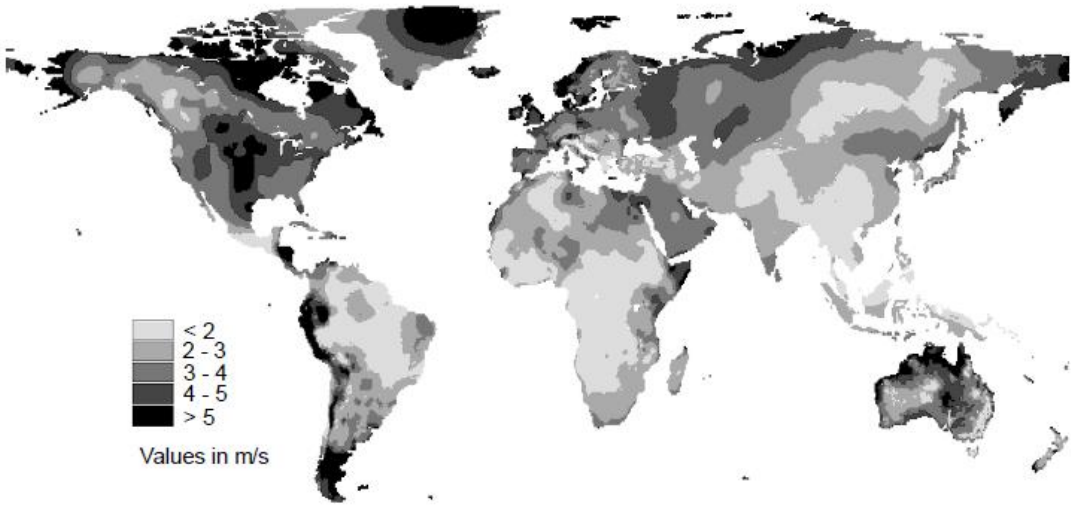

Figure 1.5: Mean world wind speed distribution at 10 m above the ground. Image taken from ref [2].

Hydropower, like wind power, has also been put to use by humans for a long time. Of the renewable energy technologies discussed, hydroelectric is currently the largest contributor of energy. Of the total solar energy incident on the earth, 21% is responsible for the water cycle. Only 0.02% of that energy contributes to water available for hydroelectric power production [2]. Most often, large scale hydropower facilities rely on an elevated reservoir of water. Water is directed down to a water turbine that converts the kinetic energy of the water to electrical energy. One of the difficulties with widespread use of hydropower is that it is a very regionally specific source of energy. Large scale hydropower typically requires damming up rivers which involves a very high initial cost, a lengthy time to plan and construct, and a significant impact on the surrounding environment.

Unlike the other renewable energy sources discussed, geothermal energy is the only that is not derived from solar energy. Geothermal energy relies on the high temperatures below the earth's surface. The most common method of converting

geothermal energy into electricity is by using the high underground temperatures to heat water and operate a steam turbine power plant. One of the major hindrances that will prevent the growth of geothermal energy is that it is highly regionally specific and costly. Geothermal power plants can only be located in areas where high temperatures are located close enough to the earth's surface, which will limit its growth as a major power producer.

Direct solar energy has significant potential to provide for the world's energy needs. Solar energy is converted to electricity in two different methods: solar thermal and photovoltaic. Solar thermal electricity generation is typically done by focusing the solar radiation to heat a fluid and operate a steam power plant [3]. The sunlight can also be converted directly to electricity by the photovoltaic effect in a solar cell. A solar panel is made up of many individual solar cells and a collection of solar panels is arranged in an array. Infrastructure for a photovoltaic solar array is relatively simple and inexpensive compared to other technologies. Solar energy is regionally specific (Figure 1.6), but much less than the technologies discussed earlier. The cost of photovoltaic power production has continued to drop in the past several decades and is approaching $1 per watt. Of the renewable technologies that are currently being pursued for large scale power production, photovoltaics have significant potential.

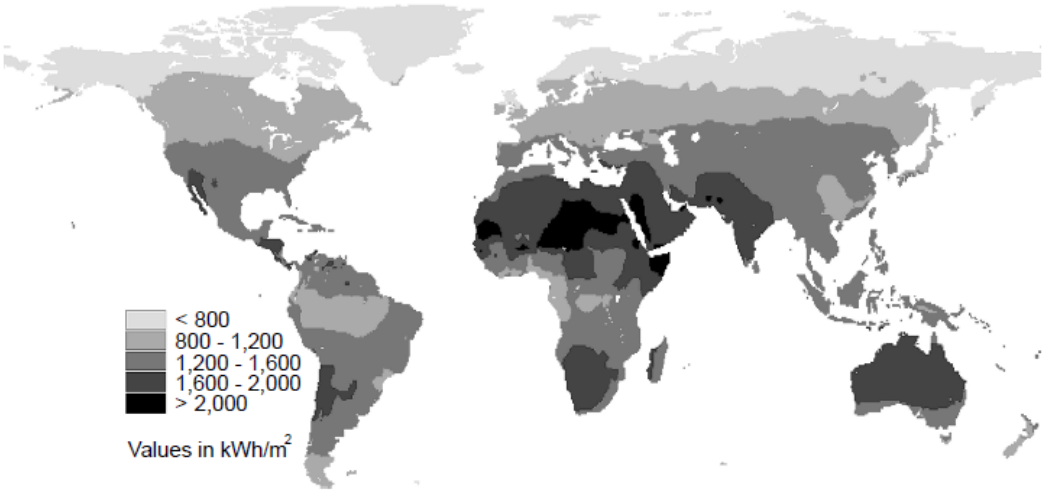

Figure 1.6: Mean values of solar radiation. Image taken from ref [2].

1.3 Basics of Photovoltaics

Photovoltaic technology allows for sunlight to be directly converted into electricity. This is achieved by the use of semiconductor materials. Band theory of solids states that electrons of atoms in solids occupy states in energy bands. Energy bands are relationships between the allowed electron energy levels and the crystal momentum and are the result of the wave functions of electrons moving through a periodic potential within a crystal lattice. Electrons will occupy states in the lowest energy bands first and then begin to fill higher energy bands. The occupied band with the highest energy, E_V, is the termed the valence band and the unoccupied band just above the valence band with energy, E_C, is the conduction band. In a perfect solid, energy states between the valence band and the conduction band are forbidden and not occupied. Material properties of solids vary widely depending on the energy band structure. Figure 1.7 shows how the band structure of conductors, insulators, and semiconductors are different.

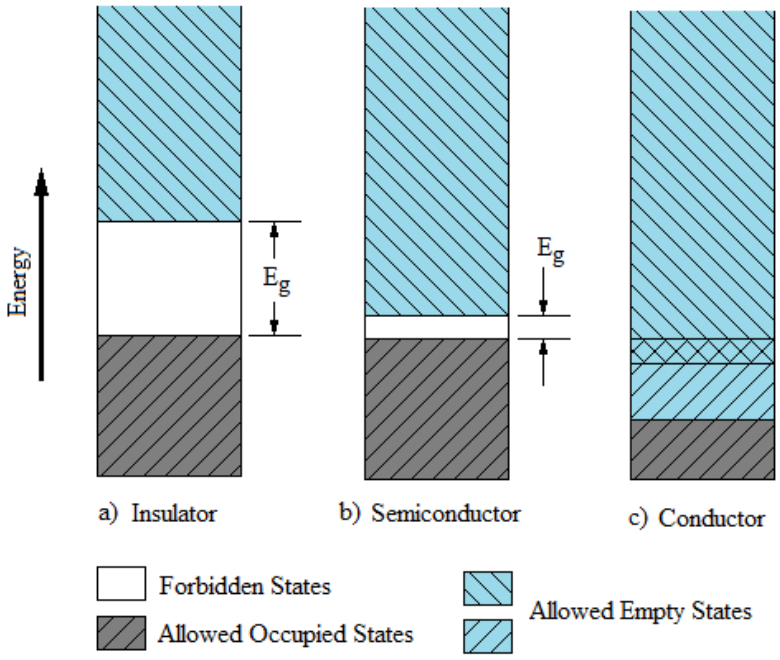

Figure 1.7: Simplified band structures of solids. a) A completely filled valence band with a large bandgap is an insulator, b) a completely filled valence band with a small bandgap is a semiconductor, c) a partially filled valence band with overlapping valence and conduction bands is a conductor.

Semiconductors are characterized by a valence band with states that are completely occupied and a small (~1 eV) band gap, E_g [4]. In a pure semiconductor, at absolute zero, no electrons are present in the conduction band and it behaves as an insulator. Increasing temperature allows for thermal energy to excite electrons into the conduction band leaving holes behind in the valence band. Excited electrons and resulting holes are called charge carriers and are the contributors to electric current. Depending on the semiconductor, the transition from the valence band to the conduction band can be either direct or indirect. The band structure of a direct band gap semiconductor is shown in Figure 1.8. For photovoltaic applications, direct band gap semiconductors are desirable.

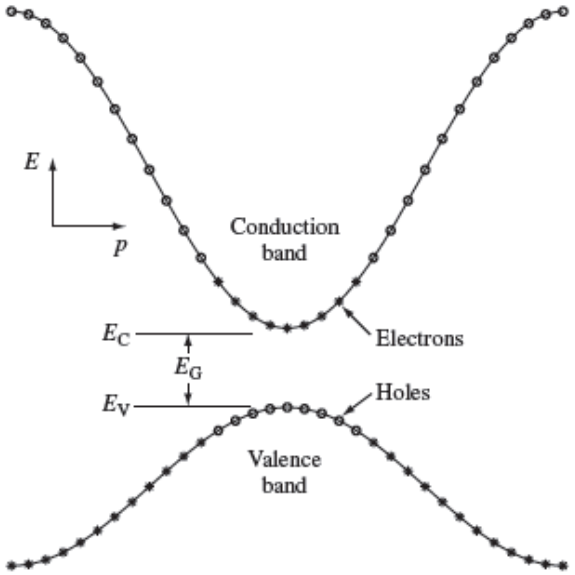

Figure 1.8: An energy band diagram for a direct band gap semiconductor. Electrons near the top of the valence band have been excited directly upwards to empty states in the conduction band. Image taken from ref [5].

In order to achieve necessary material properties, semiconductors are typically doped with impurity atoms. These impurity atoms either donate or accept electrons in the valence band. Semiconductors that have excess holes are called p-type semiconductors and those that have excess electrons are called n-type semiconductors. When p-type and n-type semiconductors are placed together they form a p-n junction. If the same material is used for the p-type and n-type of the junction it is called a homojunction and if dissimilar semiconductors are used it is called a heterojunction. Figure 1.9 shows a diagram of a p-n junction as well as the shift in energy band structure. When the junction is formed, in order to achieve equilibrium, electrons from the n-type region diffuse across the junction and recombine with holes to leave positively charged ionized donors in the n-type region and negatively charged ionized donors in the p-type region. The region

containing the ionized donors has very few free charge carries and is called the depletion region. The width of the depletion region varies depending on the doping levels, biasing, and other factors. The resulting charged donors in the depletion region will create an electric field and the corresponding voltage is called the built in voltage, V_{bi}.

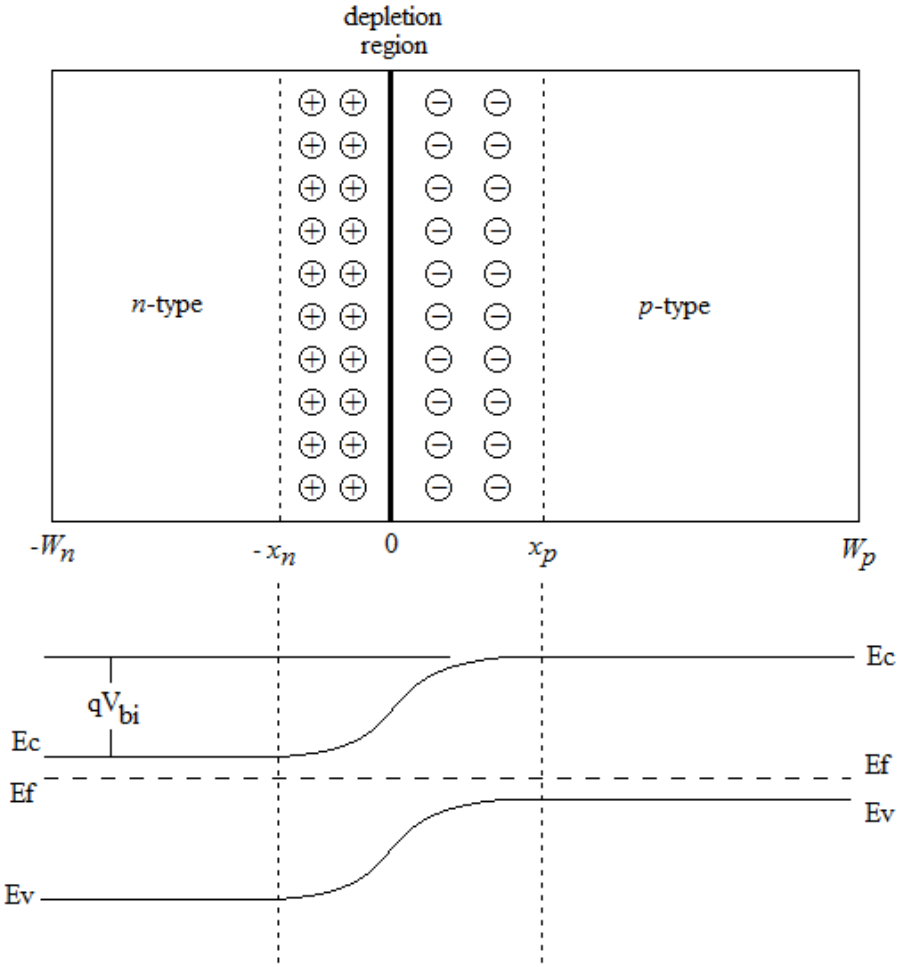

Figure 1.9: Diagram of a p-n junction.

The p-n junction is what allows solar cells to generate electric current. The electromagnetic spectrum that makes up "white light" corresponds to photons with a range of energies. Photons that have energies equal to or greater than the band gap of a

material can transfer their energy to electrons to be excited from the valence band to the conduction band. For solar cells the junction is oriented so sunlight is incident on the n-type layer. The n-type layer is called the window layer because it has a relatively high band gap compared to photons contained in sunlight. Nearly all photons pass through the n-type layer and are then absorbed in the p-type layer which has a band gap similar to the incident photons. Photons that are absorbed in or very near the depletion region produce free charge carriers (electrons-hole pairs) that are available to produce an electric current. The electric field in the depletion region sweeps electrons to the n-type side and holes are swept to the p-type side. Contacts on the front and back of the device collect these charge carriers and the resulting in an electric current. A simple circuit diagram of a solar cell is shown in Figure 1.10. The junction behaves as a current source, J_L.

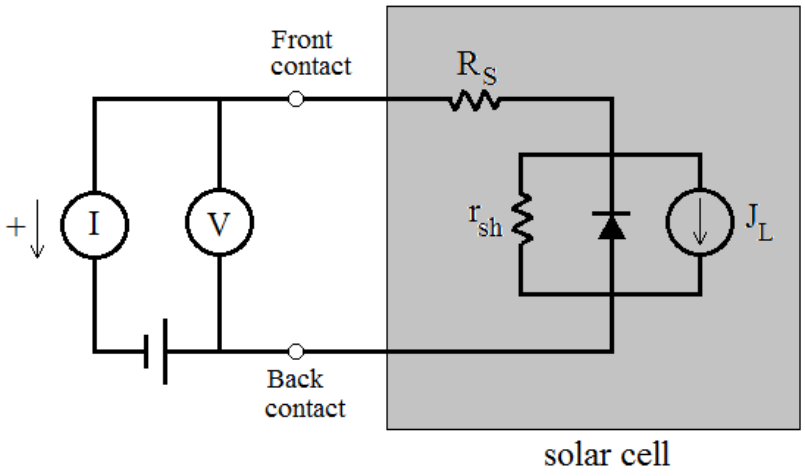

Figure 1.10: A circuit diagram of a solar cell coupled with an external load. R_S is the series resistance and r_{sh} is the shunt resistance.

Under no illumination a solar cell behaves as diode and in an ideal case the relationship of current density and voltage through the device is given by:

$$J = J_0\left[\exp\left(\frac{qV}{kT}\right)-1\right] \tag{1-1}$$

where J_0 (typically given in mA/cm^2) is the saturation current density, q is the electron charge (1.602x10^{-19} Coulomb), V is the applied voltage, k is the Boltzmann constant (1.38x10^{-23} Joules/Kelvin), and T is the temperature in Kelvin. Under illumination the current density and voltage relationship is:

$$J = J_0\left[\exp\left(\frac{qV}{kT}\right)-1\right]-J_L \tag{1-2}$$

where J_L is the current produced by the solar cell. In real world applications, the ideal equation does not apply and must be modified to include other variables:

$$J = J_0\left[\exp\left(\frac{q(V-J\cdot R_S)}{AkT}\right)-1\right]+\frac{V-J\cdot R_S}{r_{sh}}-J_L \tag{1-3}$$

where R_S is the series resistance, r_{sh} is the shunt resistance, and A is the diode quality factor. Figure 1.11 and Figure 1.12 show the effects of series resistance and shunt resistance on solar cell performance.

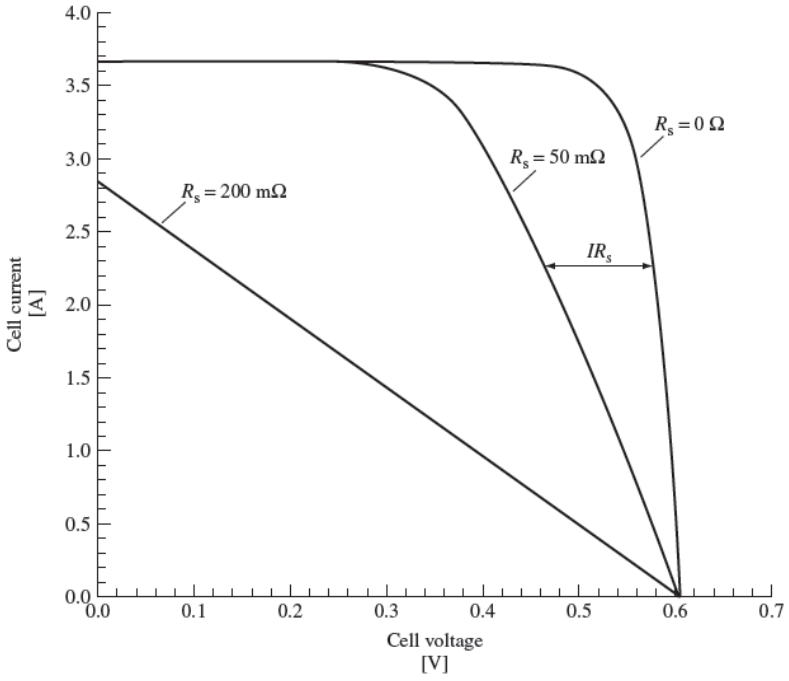

Figure 1.11: Effects of series resistance on the current-voltage behavior of a solar cell. The shunt resistance is assumed to be infinite. Image taken from ref [5].

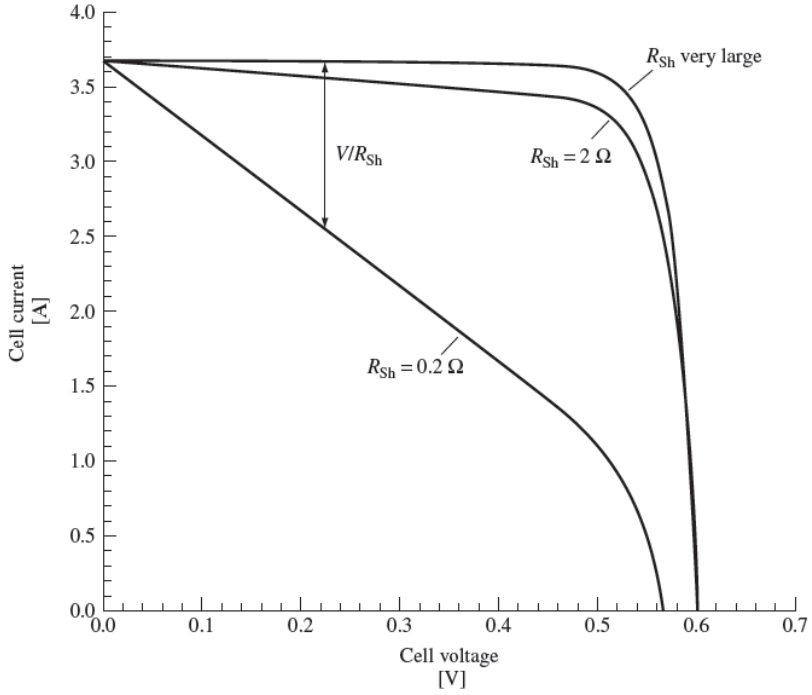

Figure 1.12: Effects of shunt resistance on the current-voltage behavior of a solar cell. The series resistance is assumed to be zero. Image taken from ref [5].

Another important concept in solar cells is that of charge carrier recombination. Recombination processes are crucial to solar cell performance. The generation of charge carriers creates a state non-equilibrium and recombination processes seek to restore equilibrium. When a photon is absorbed and an electron-hole pair is generated it is necessary that they be swept across the junction before they recombine. There are several mechanisms that are responsible for recombination. Recombination can occur through traps (defects) with energies located in the bandgap. This is also called Shockley-Read-Hall (SRH) recombination [6]. Radiative recombination or band-to-band recombination is the reverse process of optical generation where electrons drop from the conduction band to the valence band and emit photons. In Auger recombination the energy released during recombination is given to another carrier and then released as a phonon. Recombination processes are shown in Figure 1.13. Recombination mechanisms in CdTe solar cells are typically dominated by SRH recombination [7, 8].

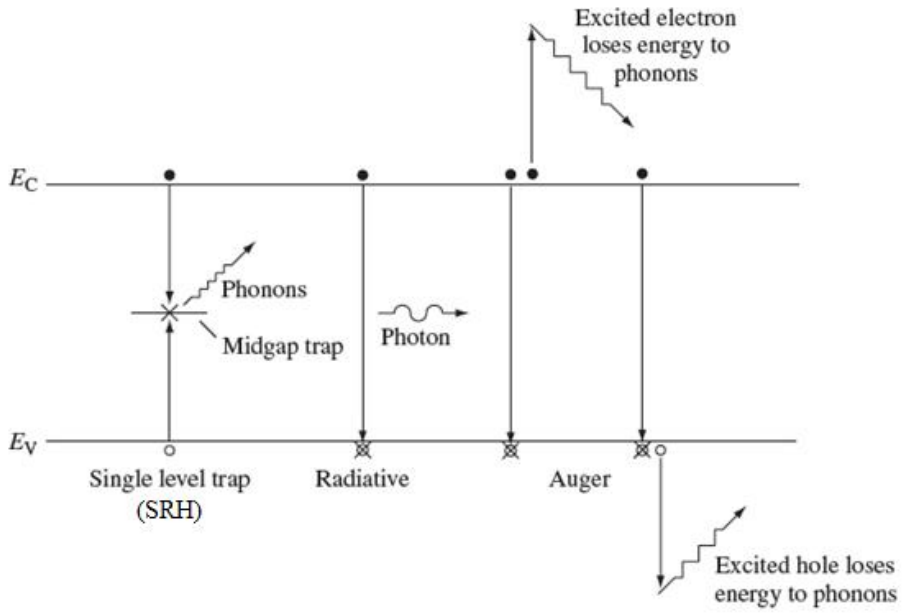

Figure 1.13: Recombination processes in semiconductors. Image taken from ref [5].

1.4 Basics of CdTe Photovoltaics

Thin-film solar cells are positioned to become the future of solar cell technology. In the current thin-film solar cell market, CdTe solar cells are proving to be a serious contender for the overall market. Over the past several decades, CdTe technology has grown significantly. Figure 1.14 shows record CdTe solar cell efficiencies as well as other leading solar cell technologies since the 1970's. The current record CdTe thin-film solar cell was made at the National Renewable Energy Laboratory with an efficiency of 16.5% [9]. While CdTe does not have the highest record efficiencies, it does have other desirable properties.

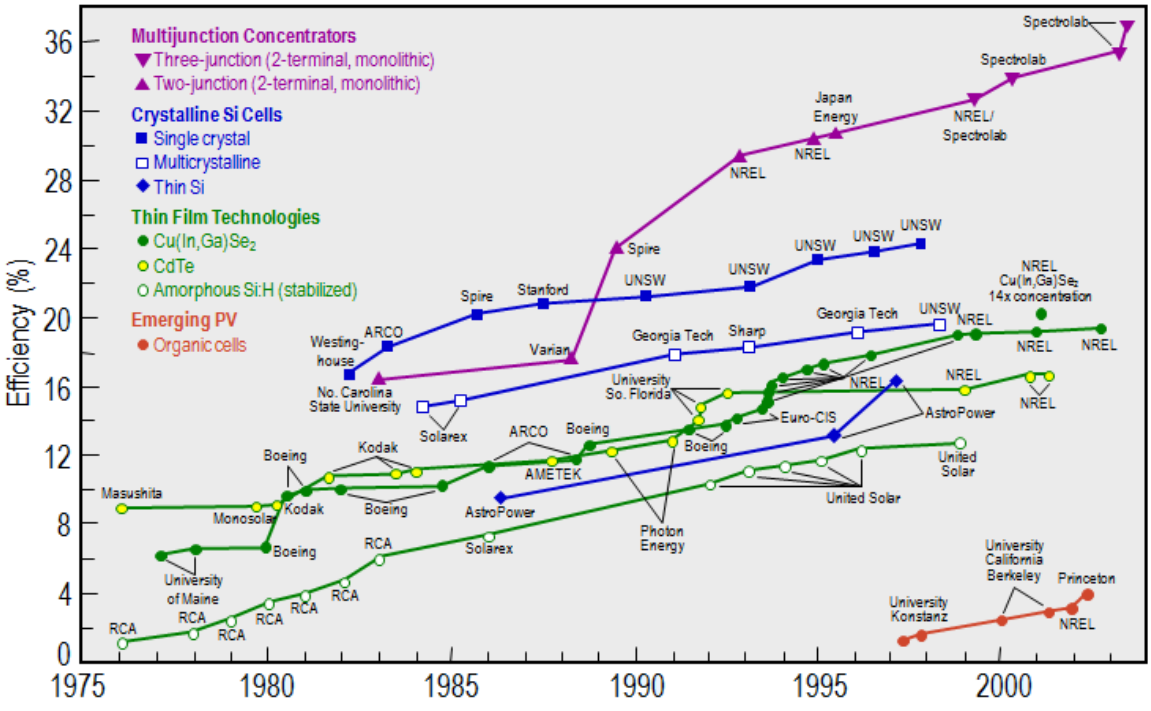

Figure 1.14: Record solar cell efficiencies over the past 25 years. Image taken from ref [10].

CdTe is a II-VI semiconductor with a direct band gap of 1.5 eV with a high absorption coefficient of $>10^5$ cm^{-1}. It is well matched to the solar spectrum and can be

expected to absorb over 90% of incident photons with energies at or above the band gap in only about 2µm of the CdTe layer which allows for thin CdTe films to be used. A CdTe abosorber layer is most often paired with CdS as the window layer of the cell. CdS has a higher band gap of ~2.5 eV which allows photons to pass through and be absorbed in the CdTe layer. The CdS layer is made as thin as possible to allow the maximum number of photons to pass through to the CdTe layer. Nearly all CdTe/CdS solar cells are manufactured in a superstrate configuration (Figure 1.15).

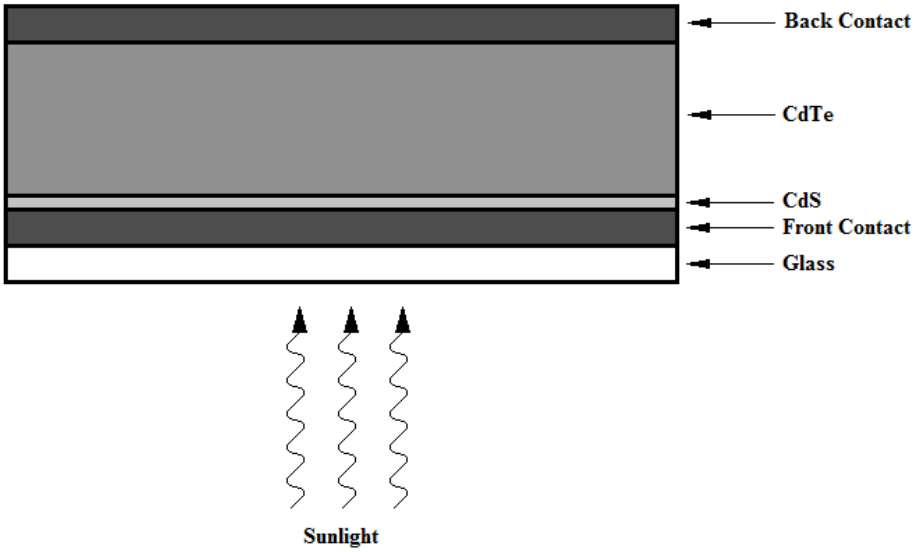

Figure 1.15: Superstrate configuration of a typical CdTe/CdS solar cell. Not to scale.

A transparent conducting oxide (TCO) is applied to the glass as a front contact. Tin oxide (SnO_2) and indium-tin oxide (In_2O_3:Sn) are commonly used. CdS and CdTe are then deposited. The method of depositing the CdS and CdTe films varies widely and can significantly affect material properties and device performance. Figure 1.16 shows some common methods of depositing CdTe layers. Among the various CdTe deposition techniques, close space sublimation (CSS) has proved to be very effective and has

produced cell with the highest efficiencies. Typical thicknesses for CdTe films are 2-10 µm and CdS layers are sub-micron thickness. Back contacts are typically formed by first creating a Te rich layer and then depositing copper followed by a graphite paste. Creating an ohmic contact with low resistance has proved to be difficult and there is tendency for a Schottky barrier to form between the p-type material and the back contact which severely impacts cell performance.

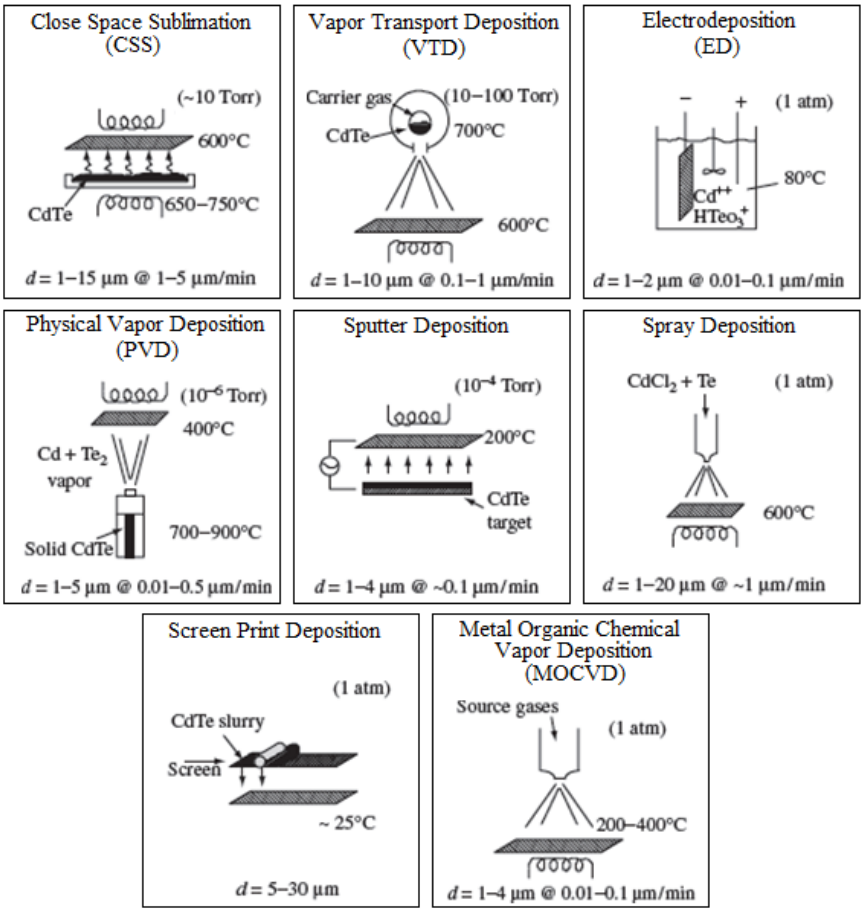

Figure 1.16: Common methods of CdTe deposition. Image taken from ref [7].

Another key advantage of using thin-film CdTe is that it allows for far less material to be used than traditional silicon solar cells. Typical silicon solar cells are made by slicing wafers of a grown crystal that are 200 µm - 400 µm thick, which is about 100

times greater than thin-film CdTe. The needed purity of CdTe needed is typically 99.999% (5N) pure [11] which is 100 times less than the needed purity of silicon solar cells. There has also been some debate about continuing progress of CdTe solar cell technology because of the toxicity of cadmium and its impact on the environment. In comparison with other leading energy producers, CdTe photovoltaics emit less cadmium per unit energy produced (Figure 1.17). As an example, a 1 m^2 CdTe panel contains less cadmium than a size C nickel-cadmium battery [12].

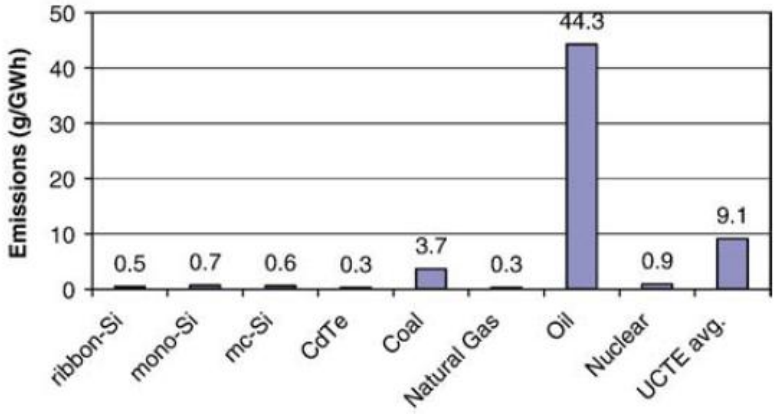

Figure 1.17: Life-cycle atmospheric cadmium emissions of different energy producers. (UCTE, Union for the Coordination of Electricity Transmission). Image taken from ref [13].

One of the biggest challenges for thin-film photovoltaics is to lower the cost per watt of energy produced. This can be done by reducing production costs as well as improving device efficiency. Costs have dropped significantly in the past several decades and are approaching the cost of other current energy sources, but there is still progress to be made. As the cost continues to drop, CdTe technology will go on to become a larger contributor to the global energy scheme.

CHAPTER 2: Experimental Details

2.1 Introduction

In order to produce quality thin-film solar cells it is necessary to measure device properties and performance on different levels. There is no one test or experiment that can give all the needed information required to accurately characterize a thin-film solar cell, so it is necessary to do a number of different characterization techniques. Using a carefully selected group of tests gives a greater understanding of the different mechanisms at work. The tests done in this study focus on different aspects of the device. It is important to compare physical characterization tests, overall performance and device processing conditions. Thin-film solar cells were manufactured at Colorado State University. Microstructural tests done in this study are X-ray diffraction (XRD), atomic force microscopy (AFM), and scanning electron microscopy (SEM). Overall performance was tested by current density-voltage (J-V) measurements. Other physical characterization was done by time-resolved photoluminescence (TRPL), laser beam induced current (LBIC), and quantum efficiency measurements (QE). The results from these tests are correlated with changes in processing conditions.

2.2 Colorado State University CdTe/CdS Thin Film Fabrication Process

Over the past two decades, the CSU Materials Engineering Laboratory has been focused on developing a simple and effective method of creating CdTe/CdS thin film solar cells. This research has not only been successful in the lab setting, but has also made a successful transition into mass production by industry [14, 15].

The system developed by the CSU Materials Engineering Laboratory utilizes a continuous, in-line design (Figure 2.1). Soda-lime glass substrates (Pilkington TEC 15, 3x3 in) are evenly place on a continuous conveyor belt that feeds them through the entire production process. The unprocessed substrates are fed though an air-vacuum-air (AVA) seal into the vacuum chamber. Once in the chamber the substrates stop at a sequence of stations for two minutes each. The substrates sequentially have a CdS layer deposition, CdTe layer deposition, $CdCl_2$ deposition and heat treatment, $CdCl_2$ annealing and stripping, and back contact creation. After this procedure the processed substrates exit the vacuum chamber through another AVA seal [16, 17].

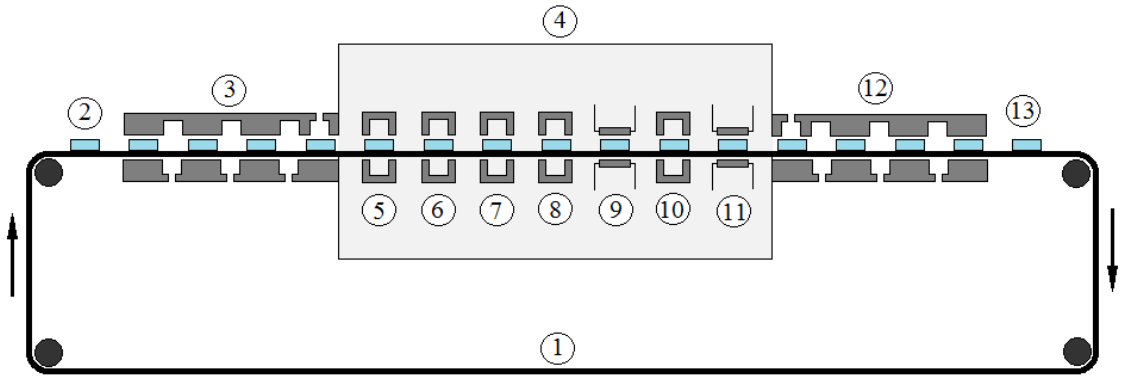

Figure 2.1: Diagram of the system used to process solar cells at CSU. (1) continuous conveyor belt (2) unprocessed glass substrate (3) AVA seal (4) vacuum chamber (5) substrate heating (6) CdS deposition (7) CdTe deposition (8) $CdCl_2$ deposition and heat treatment (9) $CdCl_2$ annealing and stripping (10) back contact creation (11) back contact annealing (12) AVA seal (13) completed device.

Thin films are deposited onto the substrates via a patented deposition method termed heat pocket deposition (HPD) (Figure 2.2) [15] which is similar to close-space sublimation (CSS) [18]. In both the HPD and CSS techniques the deposition to the substrate is controlled by heating the deposition material to a high enough temperature to sublimate it and create a vapor flux on the substrate. One of the key differences between CSS and HPD is that HPD forms a sealed pocket that contains the vapor flux. This offers a more uniform deposition and also contains each deposition station and virtually eliminates cross-contamination between sources which is the reason that only one vacuum boundary is needed [15]. The base pressure for this system is only 10^{-3} Torr which allows the use of less expensive vacuum pumps and related hardware [17]. The processing under vacuum is done with a nitrogen ambient, a small part oxygen (0.5-2%), and minimized water vapor content.

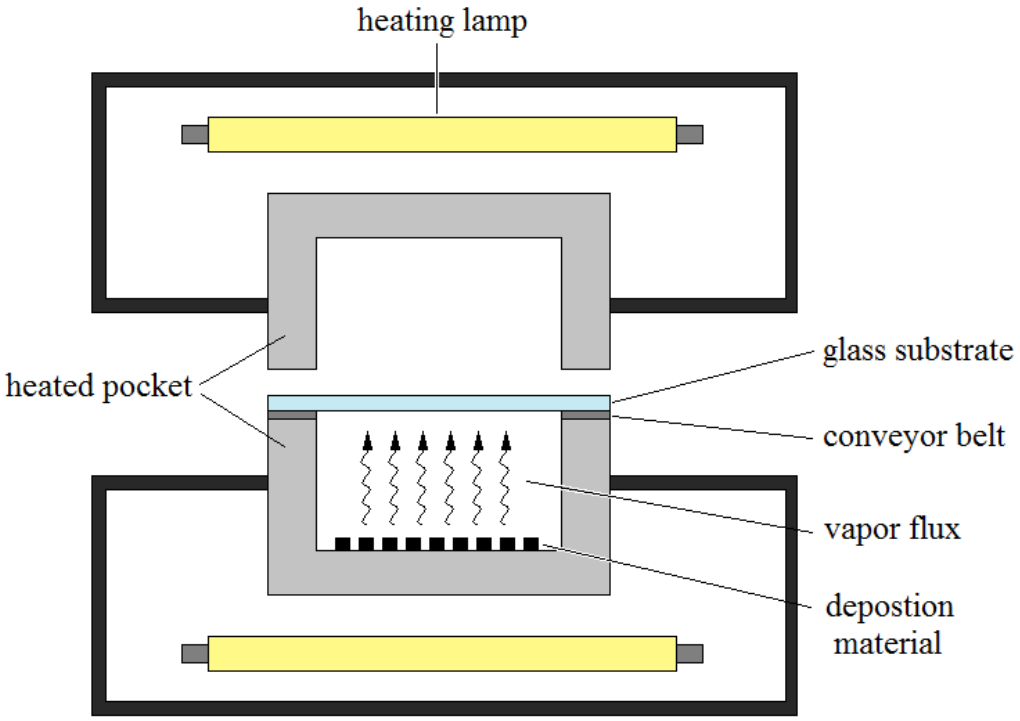

Figure 2.2: Diagram showing the HPD method for thin film deposition.

This system allows for a high level of variation of process parameters (temperature, ambient gas, process time, etc). Over the course of research at CSU, a specific set of process parameters have be established and CdTe devices have been created with efficiencies in excess of 12% [16]. The CdTe devices analyzed in this study use similar process parameters as the baseline for investigating the effects of extended $CdCl_2$ treatment. The processing times at each station are shown in Table 2.1. The samples that will be focused on in this study are those that have 2, 4 and 6 minute $CdCl_2$ treatments with 2 minutes at every other station. Due to the continuous nature of this system, holding cells for additional time at the $CdCl_2$ source caused other cells to be created with the same time delay at other stations. The top and bottom source heater temperatures are shown in Table 2.2.

Table 2.1: Description of process times for each source. The highlighted rows are the cells with 2, 4, and 6 minute $CdCl_2$ treatments.

Time at each station (min)						
Sample Name	$CdCl_2$ Source	Heater 2	$CdCl_2$ Stripping	Cu 1	Cu 2	Heater 4
238-33	2	2	0	0	0	0
238-51	2	2	2	2	2	4
238-52	2	2	2	2	4	2
238-54	2	2	2	2	2	2
238-55	2	2	2	2	2	2
238-56	2	2	2	4	2	2
238-57	2	2	4	2	2	2
238-58	2	4	2	2	2	2
238-59	4	2	2	2	2	2
238-68	6	2	2	2	2	2

Table 2.2: Source temperatures used for this study.

Source Temperatures (°C)									
	Heater 1	CdS	CdTe	$CdCl_2$	Heater 2	Zn	Cu 1	Cu 2	Heater 4
Top	570	396	343	374	390	208	123	153	200
Bottom	570	608	546	432	390	208	113	220	200

2.3 X-Ray Diffraction (XRD)

X-ray diffraction is a useful experimental technique that provides information about the crystal structure of materials. In the case of thin films, properties that can be determined are phase identification, texture coefficient (orientation), lattice parameter, coherency length and volume fraction [19]. XRD testing requires little sample preparation. The key to XRD is Bragg's law:

$$n\lambda = 2d_{hkl}\sin\theta \tag{2-1}$$

where n is an integer, λ is the X-ray wavelength, d_{hkl} is the atomic plane spacing, and θ is the angle between the X-ray beam and the sample surface. Figure 2.3 shows the model

used by Bragg's law to predict the spacing between the planes of a crystal lattice. When Bragg's law is satisfied, X-rays scattered from the crystal planes will constructively interfere at specific angles.

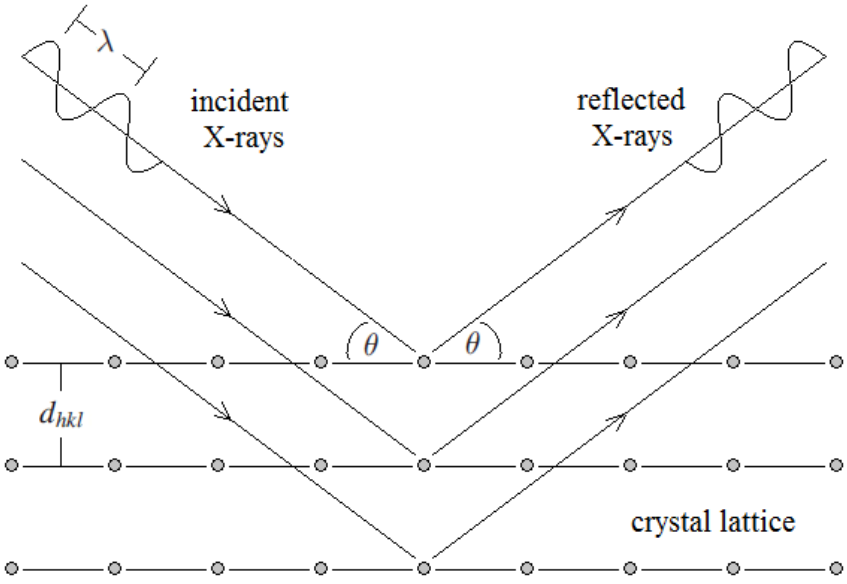

Figure 2.3: Diagram showing X-rays scattered from a crystal lattice.

An X-ray source is used to generate the incident beam. X-rays are generated by accelerating electrons through an electric potential, and impacting them on a metal target. These electrons knock out electrons from the atomic shells of the target metal. When electrons of higher energy drop down to fill these vacant states, X-rays are emitted. The most often used X-rays used for XRD are Kα (this refers to X-rays emitted when an electron drops from the n=2 shell to the n=1 shell) and common target metals are Cu, Mo and Cr [19, 20]. Figure 2.4 shows an example of an XRD experimental setup. For this study, XRD measurements were taken using a Bruker D-8 Discover system which uses a Cu X-ray source.

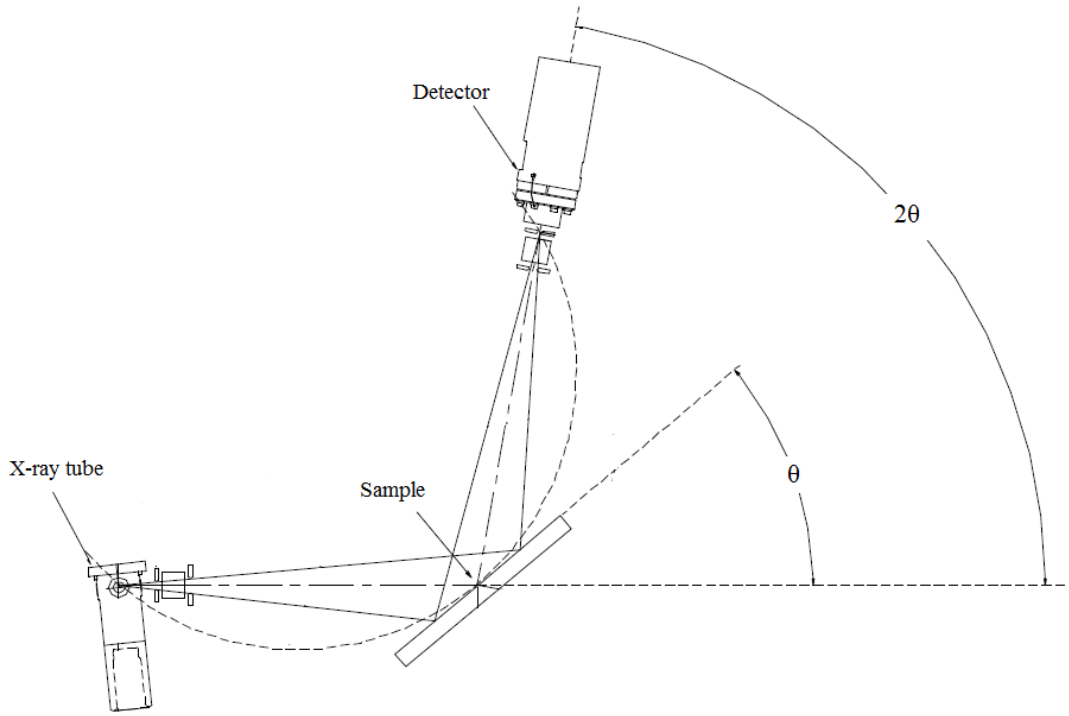

Figure 2.4: Example of an XRD setup. In this setup the X-ray source is fixed and the detector rotates around the sample.

After being scattered, the X-rays are collected by a detector and the intensities are recorded as a function of twice the scattering angle, 2θ. Figure 2.5 shows example spectra for a CdTe solar cell with crystal planes labeled for each diffraction peak. In order to determine which peaks correspond to which plane, software is used to compare the empirical data to standardized reference XRD spectra from the International Centre for Diffraction Data (ICDD).

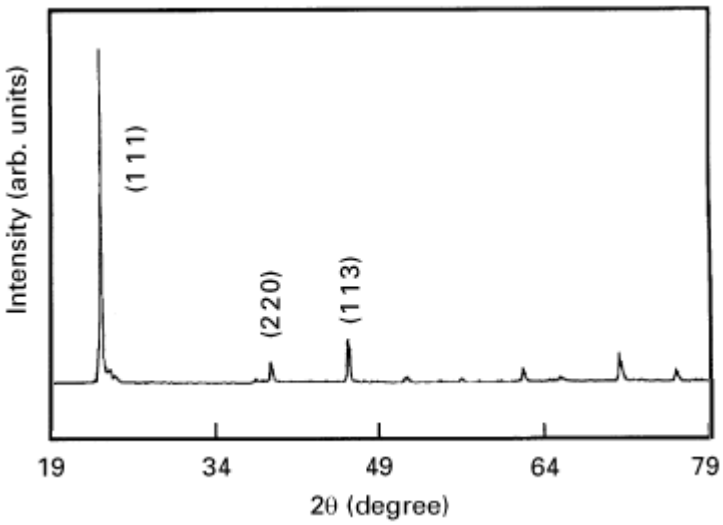

Figure 2.5: Example of XRD spectra for a CdTe solar cell with an efficiency of 10%. Image taken from ref [21].

2.4 Scanning Electron Microscopy (SEM)

Scanning electron microscopy provides highly magnified images of objects. It is able to provide much higher magnification than traditional optical microscopes. SEM utilizes a focused electron beam (~0.1 nm) to scan the surface of a sample and produce an image. SEM is able to provide magnification in excess of 100,000X, where optical microscopes are limited to around 1,500X. This is due to the fact that the wavelength of electrons is much smaller than the wavelength of photons ($\lambda_{electron}$ = 0.01nm, λ_{photon} = 400 nm-700 nm) and the depth of field is much higher for SEM. The major components of a modern SEM are the electron gun, lens system, scanning coils, electron collector, and cathode ray tube (CRT) display [22]. A diagram of a typical SEM setup is shown in Figure 2.6.

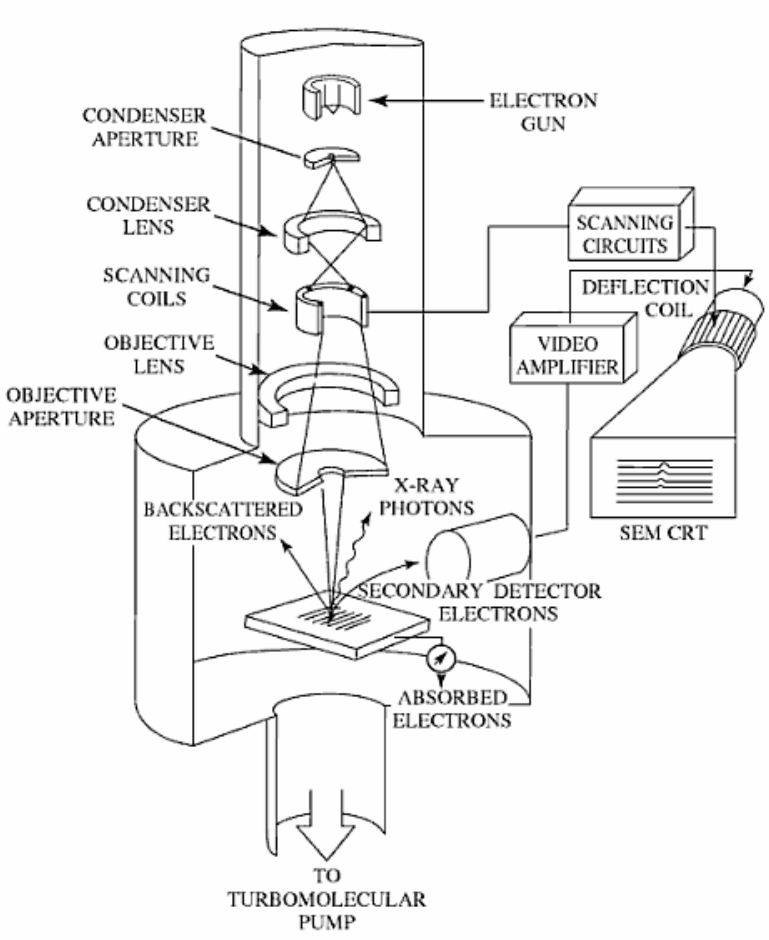

Figure 2.6: Diagram of a typical scanning electron microscope. Image taken from ref [22].

Electrons can be produced by a tungsten source, lanthanum hexaboride (LaB_6) source, or by a field-emission gun, which is the brightest and longest lasting. The electrons are focused though a set of lenses and scanning coils move the beam across the sample. The electrons incident on the sample can produce secondary electrons, backscattered electrons, x-rays, and can also be absorbed. Typically, secondary electrons are detected and used to form an image, but backscattered electrons and emitted x-rays can also be detected and used to gather information about the sample. Secondary electrons are attracted to the detector and directed to a photomultiplier which drive the CRT display and create an image.

SEM provides important visual data for thin film PV devices. The image of a cross-section of a device can give the thicknesses of different layers, the condition of the various interfaces, and the quality of the layers. A JOEL JSM 6500 with a thermal field emission electron gun was used for this study.

2.5 Atomic Force Microscopy (AFM)

Atomic force microscopy is a technique used to investigate the surface of materials. AFM can provide high resolution images of the surface topography as well as values for surface roughness. AFM uses a very fine probe (Figure 2.7) to scan the surface of a sample. The probe is located at the end of a cantilever and they are typically made silicon, silicon oxide, or silicon nitride [22].

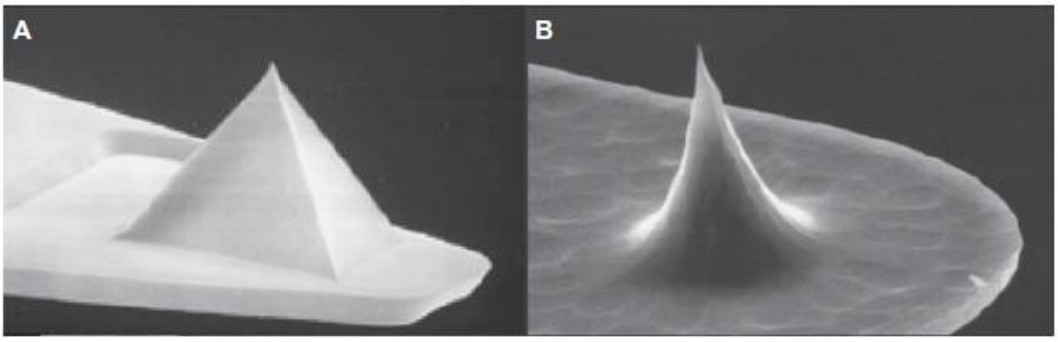

Figure 2.7: SEM images of AFM probes. a) Pyramidal probe b) Conical high aspect ratio probe for high resolution images. Image taken from ref [23].

Figure 2.8 shows an example of an AFM setup. Depending on the type of AFM used, either the cantilever is scanned over the stationary sample or the sample is moved and the cantilever is fixed. A common method to monitor the motion of the cantilever as it scans across the sample is to use laser focused at the back of the cantilever that has

been made reflective with a thin layer of gold or aluminum. As the probe moves, the laser is reflected to different positions on a photodiode. This data is recorded as the sample is scanned and a picture is created.

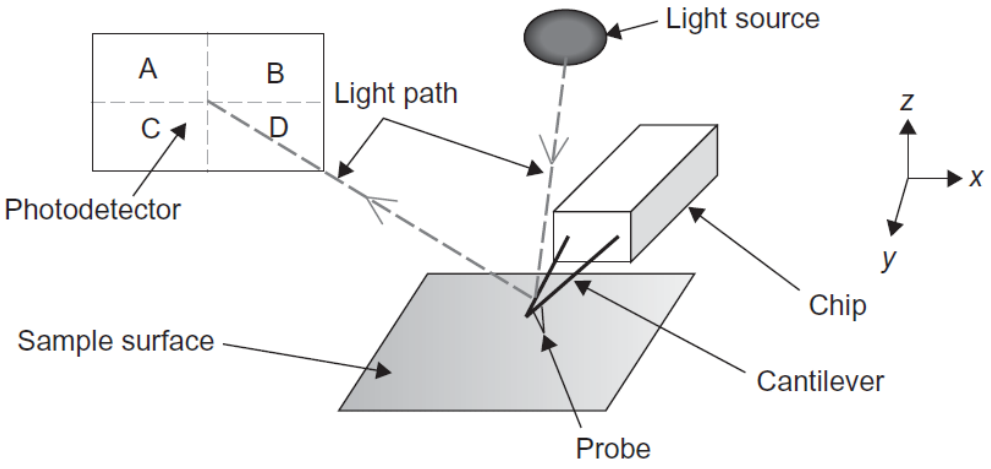

Figure 2.8: Diagram of an AFM setup. Image taken from ref [22].

The cantilever can be scanned across the surface in several different manners. It can be done in contact mode where the tip is essentially dragged across the surface of the sample. For many sample types this method works well, but for others, the dragging of the tip, along with adhesion forces between the tip and the sample can lead to tip and sample damage. Another method to scan is a non-contact mode. With this technique the tip does not contact the surface but relies on van der Waals forces to displace the cantilever. Because the van der Waal interaction is very weak, the tip must be oscillated to detect surface topography and leads to low resolution mapping. Another method combines contact and non-contact modes is called the tapping mode. In this mode the cantilever is oscillated near its natural frequency. As it comes into contact with the

sample surface, the amplitude of oscillation reduces. The sample height is adjusted to maintain a constant amplitude and can be used to create an image of the surface.

2.6 Current Density-Voltage Measurements (J-V)

Current density-voltage (often referred to simply as current-voltage) measurement is the one of the most fundamental methods of characterizing the performance of a solar cell. The cell efficiency, fill factor, open circuit voltage, and short circuit current density are determined for J-V testing. A cell is connected in series to a power supply and an ammeter (Figure 2.9). A voltmeter is also connected to the contacts of the cell. In order to easily connect the solar cell and prevent damage, a custom cell mount was used in this study that delicately made connection with the front and back contacts of the cell and had more robust terminals for electrical equipment to connect. The power supply, voltmeter, and ammeter are interfaced with a computer equipped with data acquisition software.

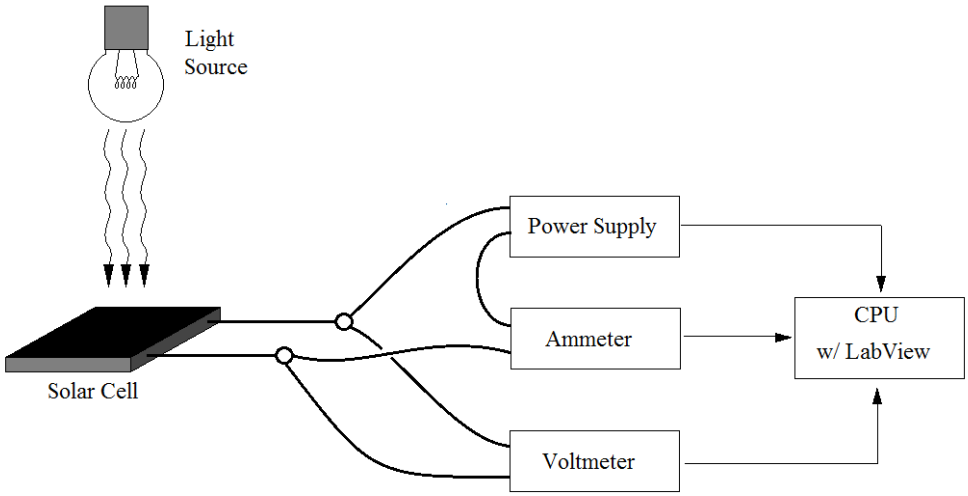

Figure 2.9: Simplified diagram of a current density-voltage testing setup.

The cell is subjected to a range of voltages, usually in the range of -0.5 V to 1 V. This is done with the cell illuminated as well as with the cell in the dark. A standard light spectrum and intensity is used to characterize solar cells. The standard is a light intensity of 100 mW/cm^2 with an air-mass 1.5 (AM1.5) light spectrum [5]. Figure 2.10 shows a typical current-voltage curve of an illuminated cell.

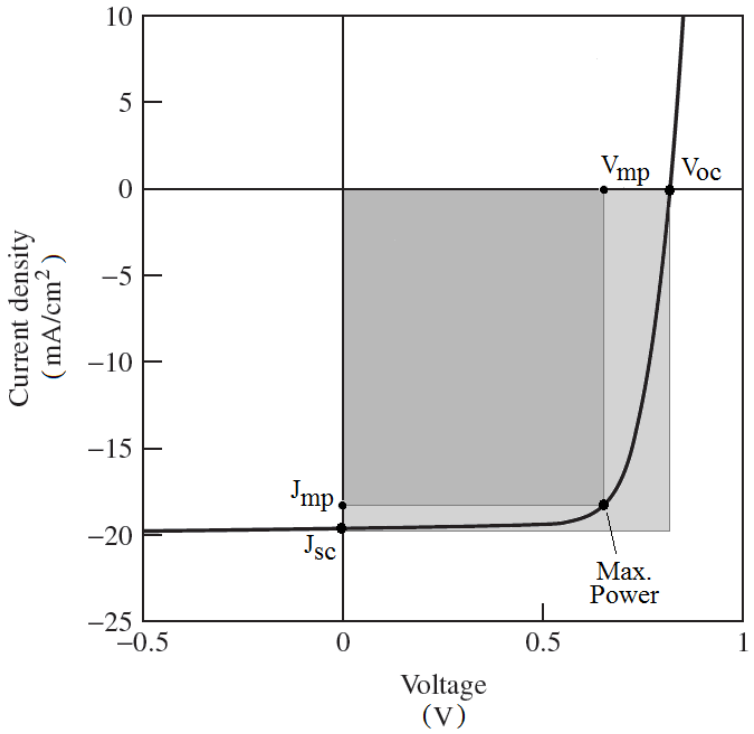

Figure 2.10: An example of a current-voltage curve. Short circuit current density (J_{SC}), current density at maximum power (J_{MP}), open circuit voltage (V_{OC}), and voltage at maximum power (V_{MP}) are labeled. The shaded areas are those used to calculate the fill factor.

From this curve the short circuit current density (J_{SC}), current density at maximum power (J_{MP}), open circuit voltage (V_{OC}), and voltage at maximum power (V_{MP}) can be found. From these values the fill factor, or "squareness" of the J-V curve can be found from the following equation:

$$FF = \frac{(V_{MP})(J_{MP})}{(V_{OC}) \cdot (J_{OC})} \tag{2-2}$$

The cell efficiency can also be calculated:

$$\eta\,(\%) = \frac{(V_{OC})(J_{SC})(FF)}{P_{IN}} \times 100\% = \frac{\text{max power out}}{\text{max power in}} \tag{2-3}$$

As an example, the current record CdTe solar cell developed at NREL has a V_{OC} = 0.845 mV, J_{SC} = 25.88 mA/cm^2, and FF = 75.51% [9]. Using these values and setting P_{IN} to the standard testing light intensity of 100 mW/cm^2, the efficiency can be calculated:

$$\eta\,(\%) = \frac{(0.845\,\text{mV})(25.88\,\text{mA/cm}^2)(0.7551)}{100\,\text{mW/cm}^2} \times 100\% = 16.5\% \tag{2-4}$$

2.7 Time-Resolved Photoluminescence (TRPL)

Time-resolved photoluminescence measurements record the photoluminescent intensity of a sample as a function of time. TRPL can be used to measure the minority carrier lifetime in thin film solar cells and nearly all direct lifetime measurements on CdTe have been done using TRPL [19]. Most often TRPL measurements are done by subjecting the sample to a pulse of light to excite free carriers. Photons are absorbed by the electrons and cause them to increase in energy and occupy empty states in the valence band and leave holes in the valence band. This causes an imbalance of carriers. The

amount of time that these free carriers exist before they recombine to reach equilibrium (by various mechanisms) and emit photons is what is measured. Photons are measured by time-correlated single photon counting [24]. Figure 2.11 shows a simplified diagram of a TRPL setup.

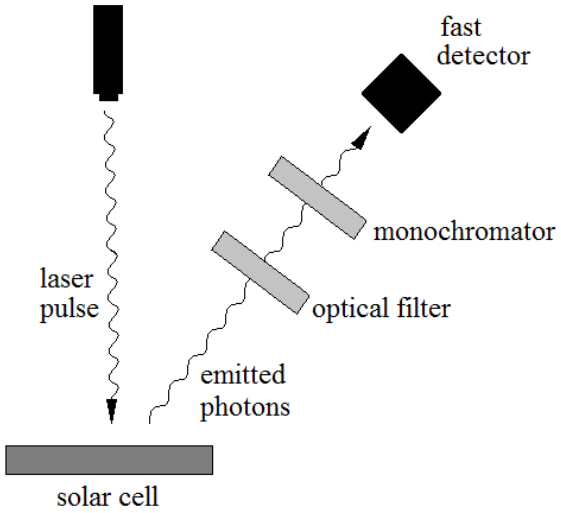

Figure 2.11: Simplified diagram of a TRPL measurement setup.

The photoexcitaion of carriers is done by a fast pulse laser tuned to a certain wavelength with a repetition rate on the order of 1 MHz. For CdTe/CdS solar cells, the light beam passes through the CdS layer and generates carriers primarily in the first 500 nm of the CdS/CdTe metallurgical junction [25]. The most widely used method of detecting the emission from the sample is time-correlated single-photon counting [26].

TRPL measurements for this study were conducted at NREL with the help of Wyatt Metzger and Darius Kuciauskas. For this study, a 650 nm laser with a continuous wave power level of 2.5 mW with a repetition rate of 1 MHz and pulse width of 5 ps.

2.8 Quantum Efficiency (QE)

Quantum efficiency measurements quantify the spectral response of a solar cell, which is critical to the performance of the cell. The quantum efficiency is defined as:

$$QE(\lambda) = \frac{\text{number of electrons collected}}{\text{number of photons incident}} \tag{2-5}$$

In order to produce a QE curve, light is focused on a portion of the test cell, the wavelength of light is swept through a given range, and the current produced is measured and recorded as a function of photon wavelength. Ideally, the light spot that shines on the sample is large enough (1-2 mm) and in a position that can be assumed to be representative of the whole cell. A diagram of the QE measurement setup used for this study is shown in Figure 2.12.

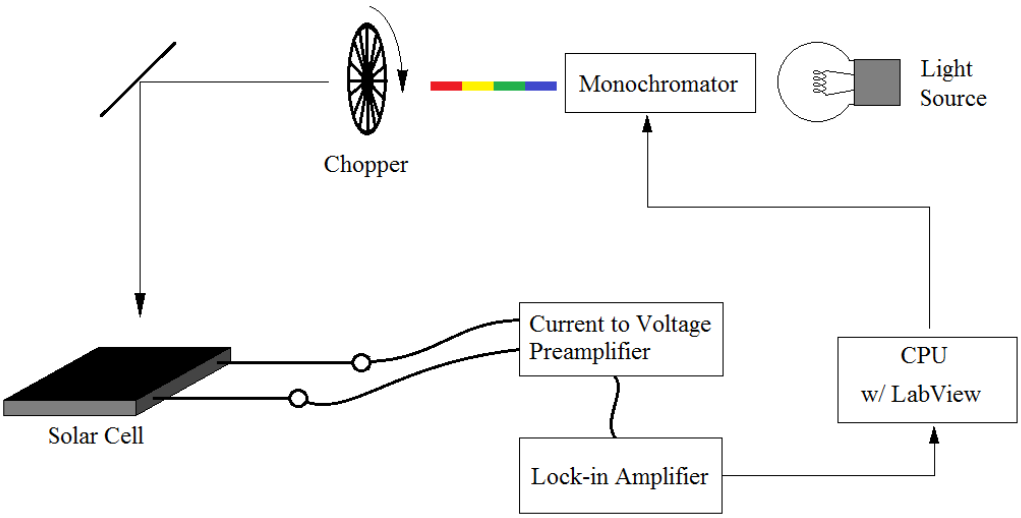

Figure 2.12: Diagram of a QE measurement setup.

The quantum efficiency measured in this study is external quantum efficiency, which includes all the effects that occur externally to the device. Internal quantum efficiency only considers photons that are incident on the junction of the device, and is always higher than the external QE value.

2.9 Laser Beam Induced Current (LBIC)

Laser beam induced current is similar to QE measurements, but instead measuring the average quantum efficiency of the cell, this technique scans a solar cell with a localized light beam. This allows a map of the quantum efficiency of the cell to be produced. Unlike QE measurements that focus light on a portion of the cell and sweep through a range of wavelengths, LBIC uses a fixed wavelength and scans over positions. This is technique is well suited to evaluate the spacial effects of different processing methods. This study used an LBIC setup at the CSU Photovoltaics Laboratory [27]. A diagram of this device is shown in Figure 2.13 and a detailed description is available from Hiltner [28].

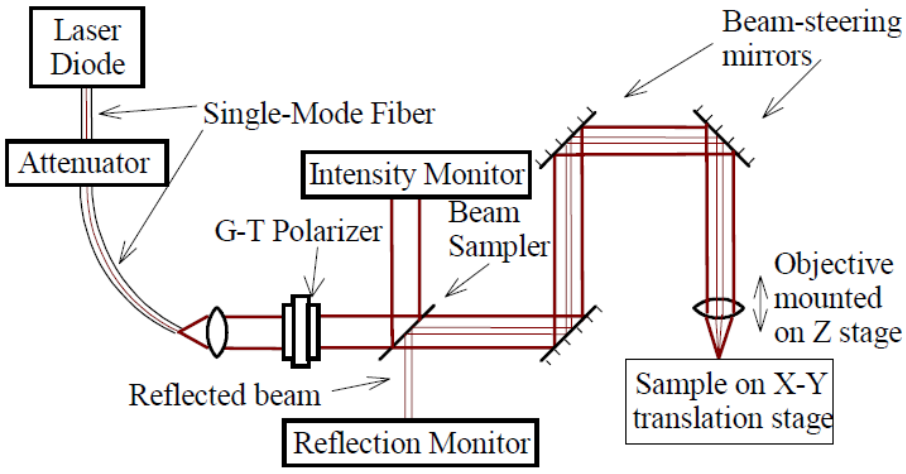

Figure 2.13: Diagram of the light beam induced current setup used. Image taken from ref [28].

The light source used for this study was tuned to 638 nm (photon energy = 1.94 eV), but has the ability for wavelengths of 685 nm, 788 nm, and 825 nm – 860 nm. The laser beam power is controlled by an optical attenuator is guided through a

Glan-Thompson polarization optic and is then guided through a set of mirrors and is sampled for beam intensity and also for reflection back from the sample. The beam is focused by a precision objective lens which allows for beam spots sizes on the sample of 100 µm -1 µm in diameter. In order to produce the scanned image, the beam is fixed and the sample stage is scanned through the beam by stepper motors. As the stage scans through the laser, induced current values are sent to a computer with data acquisition software where they are recorded and QE maps are created.

2.10 Conclusion

Solar cell characterization is a necessary to refine technology and develop high efficiency devices. The experimental techniques described were carried out on CdTe solar cells manufactured at CSU. A summary of the characterization techniques used in this study is shown in Table 2.3. Results and discussion are provided in Chapter 3.

Table 2.3: Summary of characterization techniques used in this study.

Characterization Technique	Characterization Type	Measured Parameters
X-ray Diffraction	Microstructure	prefered orientation, lattice parameter
Atomic Force Microscopy	Microstructure	topography imaging
Scanning Electron Microscopy	Microstructure	cross-section imaging
Current Density-Votage	Performance	open circuit voltage, short-circuit current, fill factor, efficiency
Time-Resolved Photoluminescence	Performance	minorty carrier lifetime
Laser Beam Induced Current	Performance	fixed wavelength quatum efficiency mapping
Quantum Efficiency	Performance	variable wavelength average quantum efficency

CHAPTER 3: Effects of $CdCl_2$ Treatment on Device Microstructure and Performance

3.1 Introduction

One of the key steps in the creation of high efficiency CdTe solar cells is a post-CdTe deposition heat treatment with $CdCl_2$. There has been a considerable amount of research done in the past several decades to determine the mechanisms by which the $CdCl_2$ treatment improves device performance as well as the best way to carry out the treatment.

The effects of the $CdCl_2$ treatment can vary depending on CdTe depositon techniques and manner in which the treatment is done. Table 3.1 highlights some of the different $CdCl_2$ treatments that have been performed by different studies. In general, the treatment involves depositing a thin layer of $CdCl_2$ and the following with annealing step. One popular method is to dip the CdTe layer in a heated solution of $CdCl_2$ and methanol (CH_3OH). After being dipped it is dried and a $CdCl_2$ film is precipitated on the surface. An issue with this technique is that it is difficult to control the concentrations in the $CdCl_2$/methanol bath [29]. Another often used method is a vapor $CdCl_2$ treatment. This technique exposes the CdTe layer to a flux of $CdCl_2$ vapor to form a thin layer. A subsequent annealing step is done. The vapor $CdCl_2$ allows for greater control of $CdCl_2$

Table 3.1: Summary of different $CdCl_2$ treatment methods.

Method of $CdCl_2$ treatment	CdTe Deposition Method	Results / Comments	Citations
Vapor $CdCl_2$	Close Space Sublimation	Many high efficiency (>10%) cells use this technique, more controllable than "wet" techniques, no grain growth, increase minority carrier lifetime, S and Te interdiffusion	[30], [8], [31], [32], [29], [33]
Vapor $CdCl_2$	Physical Vapor Deposition	Similar as above, but with substantial grain growth	[30]
Vapor $HCFCl_2$ (Freon)	Close Space Sublimation	Similar results to $CdCl_2$ treatments, less toxic than $CdCl_2$, suitable for any type of CdTe device, efficiency up to 16%	[34]
$CdCl_2$:CH_3OH solution	Close Space Sublimation	No grain growth, increased minority carrier lifetime and QE response, difficult to maintain solution concentrations, efficiency ~9%	[35], [36], [29], [37], [38]
$CdCl_2$:CH_3OH solution	Physical Vapor Deposition	Promotes grain growth, increased minority carrier lifetime and QE response, Te and S interdiffusion, efficiency ~10%	[39], [36], [37], [40]
$CdCl_2$:CH_3OH solution	Sputtering	Formation of bubbles at CdTe surface, increased minority carrier lifetime, grain growth	[40]
Vapor HCl	Thermal Evaporation	Produces $CdCl_2$ film, promotes grain growth, sensitive to HCl concentration and treatment temperature, efficiency ~1.5%	[41]
Vapor Cl_2	Close Space Sublimation	Produces a non-uniform $CdCl_2$ film, difficult to control reaction parameters, efficiency ~8%	[42]
$MnCl_2$:C_5H_5N solution	Close Space Sublimation	Poor performance, increased resistance, grain growth, efficiency ~1%	[43]
In Situ $CdCl_2$	Close Space Sublimation	$CdCl_2$ mixed with CdTe during deposition, grain growth, sensitive to $CdCl_2$ concentration, CdS diffusion leads to shunting, efficiency ~8%	[44]
$CdCl_2$ in slurry	Screen Print	$CdCl_2$ mix in with CdTe screen print slurry, efficiency ~8%	[45]

film deposition and is the process used in this study as well as many other makers of high-efficiency CdTe devices. Other $CdCl_2$ treatments include vapor HCl, vapor Cl_2, $MnCl_2$:C_5H_5N solution, $CdCl_2$ mixed with CdTe screen print paste, and in-situ $CdCl_2$ treatment.

This study combines CSS-like CdTe deposition with vapor $CdCl_2$ treatment, which is one of the leading ways to produce quality devices. With this in mind, it is important that research be done to investigate and refine the $CdCl_2$ treatment. There are many process parameters that must be carefully controlled and monitored during the treatment including, ambient gas concentrations, source temperatures, substrate temperatures, deposition time, annealing time, and others. The process for manufacturing CdTe solar cells developed at CSU utilizes a 2 minute $CdCl_2$ deposition time. While this treatment time has produce high quality devices, it is necessary to investigate the effect of varying this parameter on solar cell performance.

One of the main effects of the $CdCl_2$ treatment on electrical properties is that the Cl introduced forms an acceptor complex with Cd vacancies [7]. The $CdCl_2$ treatment is also believed to passivate grain boundary defects which act as recombination sites within the CdTe band gap [37]. This is evident by an increase in minority carrier lifetime after treatment [8, 38, 46].

It has also been shown that the $CdCl_2$ treatment promotes intermixing of the CdS and CdTe layers [32] and sulfur diffusion from the CdS layer into the CdTe [8]. The formation of $CdTe_{1-x}S_x$ and $CdS_{1-y}Te_y$ alloys at the CdS/CdTe interface leads to consumption of the already thin CdS layer and can significantly affect device performance [29, 32]. Significant sulfur diffusion will only occur in the presence of a

CdS layer and a treatment of $CdCl_2$ and heat. A treatment of only heat will not prompt any major sulfur diffusion, as shown in Figure 3.1. It has also been shown that conducting a high temperature anneal to the CdTe layer prior to the $CdCl_2$ will greatly reduce the amount of sulfur diffusion from the CdS layer [47]. The high temperature anneal prior to the $CdCl_2$ treatment promotes further recrystalizaiton of the CdTe layer which reduces the volume of grain boundaries which act as diffusion paths.

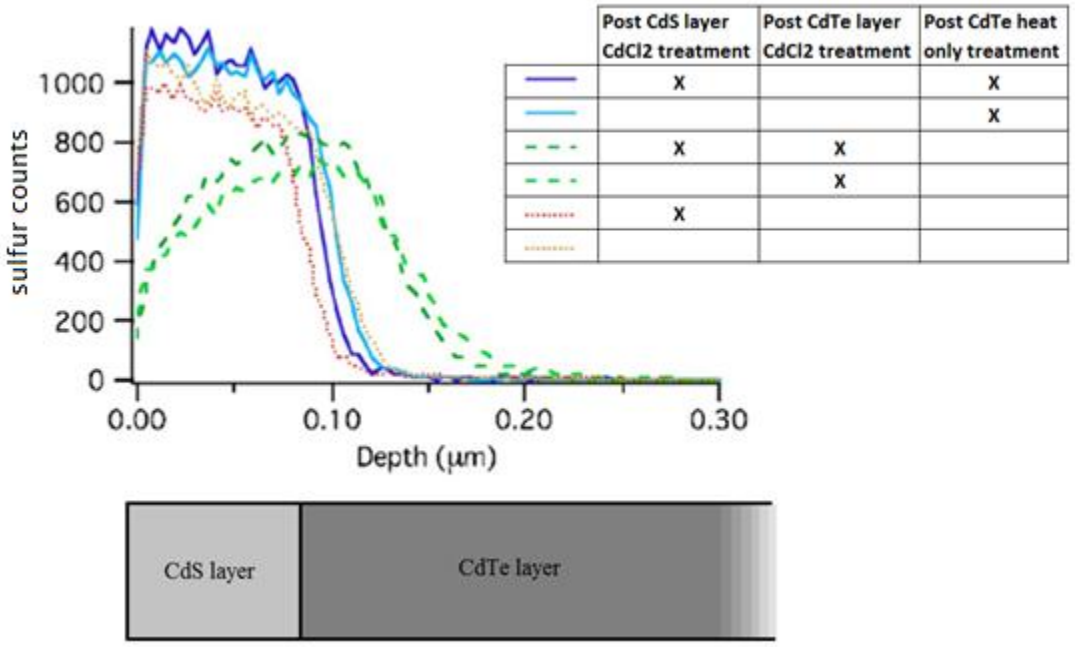

Figure 3.1: Secondary ion mass spectroscopy (SIMS) of sulfur content of a CdS/CdTe junction subjected to different treatment processes. Image taken from ref [8].

Depending on the method of deposition of the CdTe, the $CdCl_2$ can promote grain growth, recrystallization, and change the degree of preferred orientation [7]. It has been proposed that the chlorine diffusion into the CdTe lattice in the early stages of treatment creates additional defects at grain boundaries which creates lattice strain and initiates the recrystallization process [46]. As can be seen in Table 3.2, some deposition methods (PVD, ED, Sputter, MOVCD) yield a substantial increase in grain size and change in

preferred orientation while others (CSS, Spray, VTD) do not show any considerable grain growth or change preferred orientation. A study by Moutinho highlighted the differences between CdTe layers prepared by PVD and CSS [36]. The major factors that prevent secondary grain growth during the $CdCl_2$ treatment are high CdTe deposition temperature, large initial grain size, and annealing before the $CdCl_2$ treatment [7, 29, 36].

Table 3.2: Structural changes due to $CdCl_2$ treatment of CdTe deposited by different methods. Table taken from ref [7].

Deposition Method	Film Thickness (μm)	Mean Grain Size (μm): Initial → $CdCl_2$ HT	Orientation: Initial → CdCl2 HT
PVD	4	0.1 → 1	(111) → (220)
ED	2	0.1 → 0.3	(111) → (110)
Spray	10	10 → 10	Random
Screen	12	~10	Random
VTD	4	4 → 4	Random → Random
CSS	8	8 → 8	Random → Random
Sputter	2	0.3 → 0.5	(111) → (?)
MOCVD	2	0.2 → 1	(111) → Random

$CdCl_2$ treatment also considerably improves the quantum efficiency and in turn the photocurrent generated by the cell [28, 48]. Figure 3.2 shows that the uniformity of the photocurrent generated by a fixed wavelength light source (788 nm) is greatly increased by the $CdCl_2$ treatment. The overall spectral response is also significantly increased as shown in Figure 3.3.

The increase in overall solar cell performance is generally seen by an increased short-circuit current, increased open-circuit voltage, and reduced shunting. Figure 3.4 shows J-V curves for three PVD CdTe solar cells. The cell performance is drastically

improved from no post-deposition treatment, curve (a), to a vapor $CdCl_2$ treatment, curve (c).

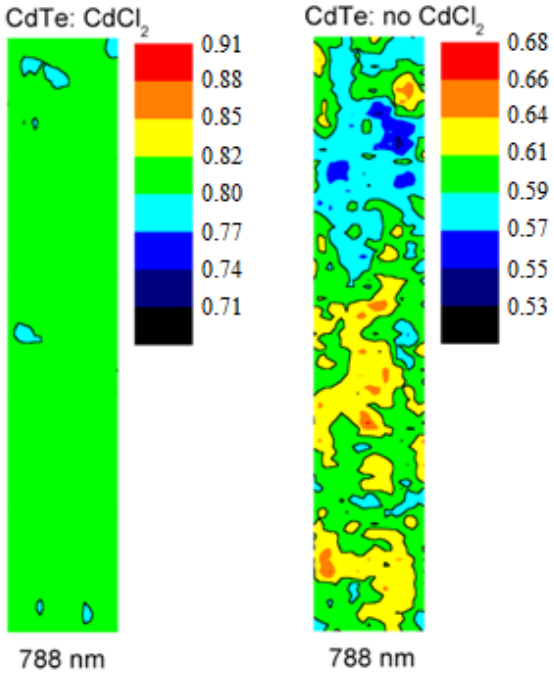

Figure 3.2: LBIC analysis of CdTe samples with and without $CdCl_2$ treatment showing changes in QE magnitude and uniformity. Image taken from ref [28].

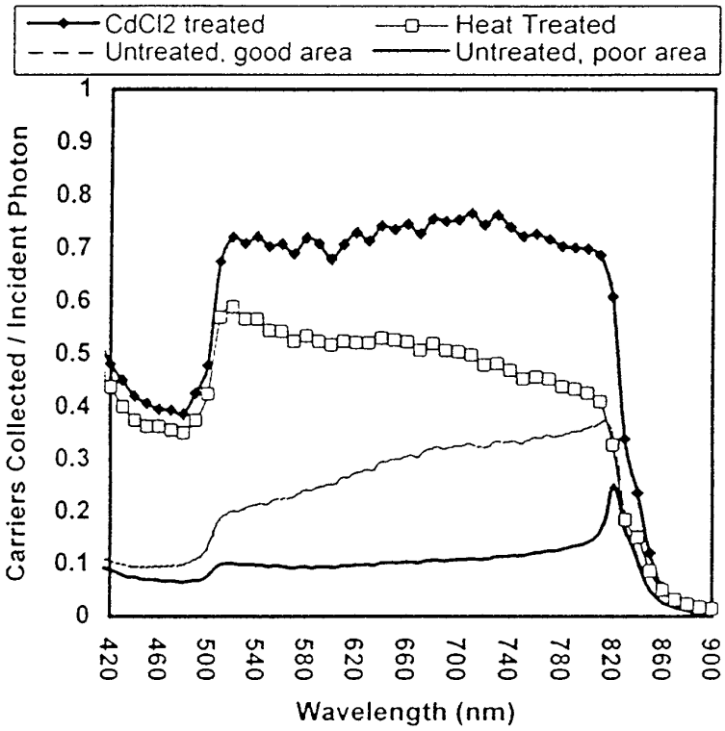

Figure 3.3: Spectral response of CdTe solar cells with and without $CdCl_2$ treatment. Image taken from ref [49].

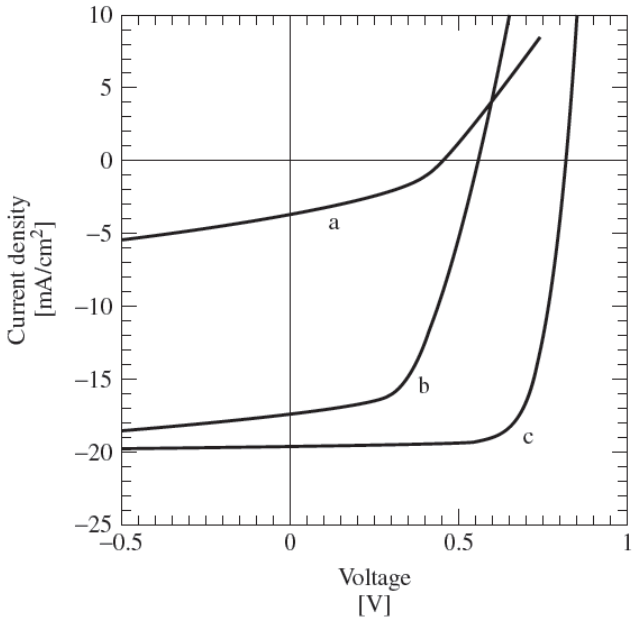

Figure 3.4: J-V curves for PVD CdTe solar cells with a) no post-deposition treatment, b) heat treatment in air only, c) heat treatment in with $CdCl_2$ vapor. Image taken from ref [7].

It is clear that the $CdCl_2$ is a necessary step to create high-efficiency CdTe solar cells. Also clear, is that the effects of the $CdCl_2$ treatment on the physical and electrical properties of CdTe solar cells are complicated. This situation is further complicated by the numerous methods in which the $CdCl_2$ treatment is conducted and its varying effects depending upon the method of CdTe deposition. Investigating and refining the process parameters of the $CdCl_2$ treatment time is of great value in the effort to produce higher efficiency CdTe solar cells. Experimental results and discussion of the tests described in Chapter 2 are presented.

3.2 XRD Results

X-ray diffraction measurements were done as described in Chapter 2. XRD spectra for each $CdCl_2$ treatment are shown in Figure 3.5 along with ICDD data for CdTe powder [50]. No significant changes are seen in XRD patterns as $CdCl_2$ treatment is increased.

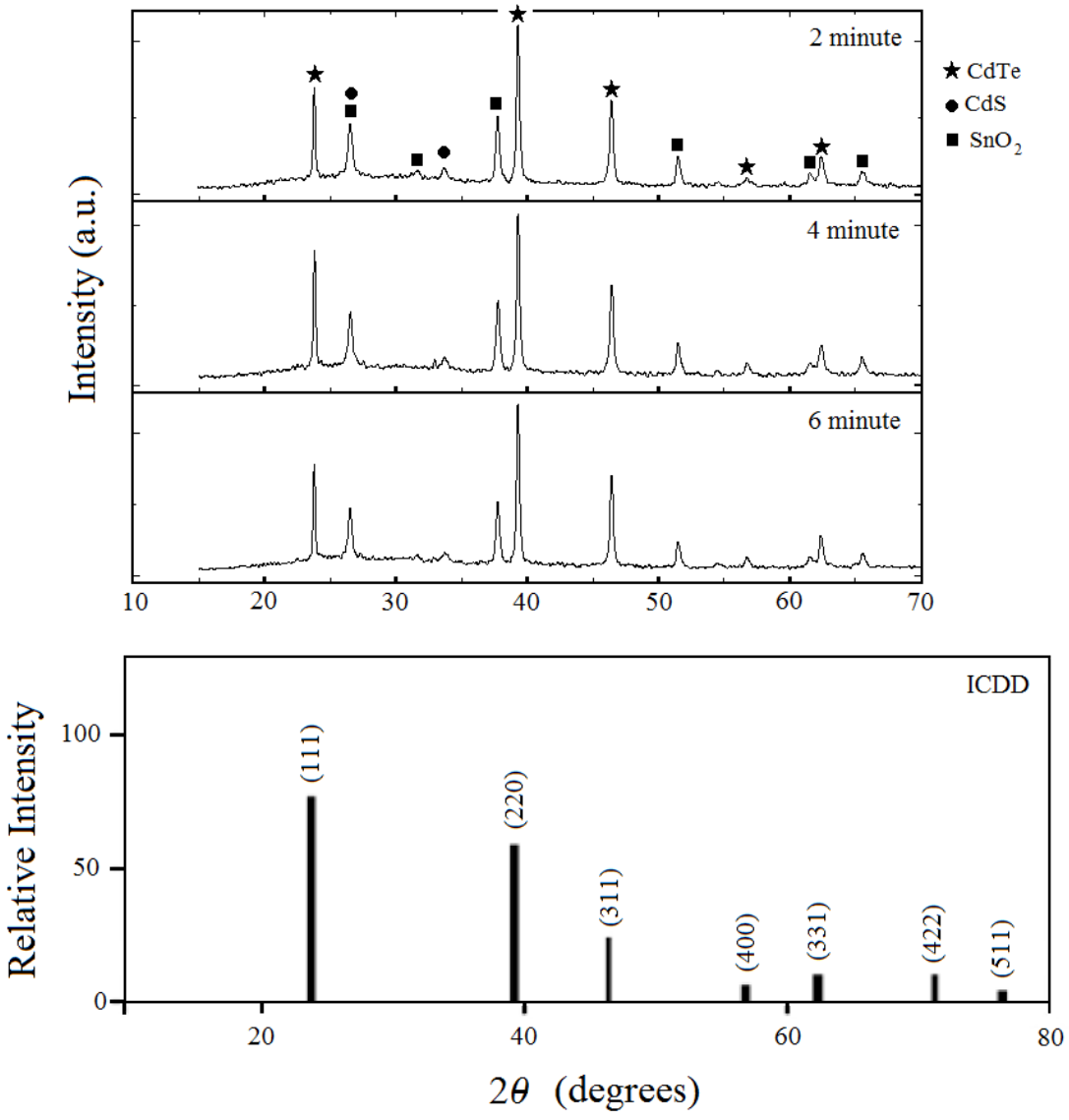

Figure 3.5: XRD of 2 min, 4 min, and 6 min $CdCl_2$ treated samples. Also shown is ICDD XRD spectra for CdTe powder.

Texture coefficients and lattice parameters of the CdTe layer were determined. Texture coefficients can be found from the following equation:

$$P(h_i,k_i,l_i)=\frac{I(h_i,k_i,l_i)}{I_r(h_i,k_i,l_i)}\left(\frac{1}{n}\sum_{i=1}^{n}\frac{I(h_i,k_i,l_i)}{I_r(h_i,k_i,l_i)}\right) \quad (3\text{-}1)$$

Where $P(h_i,k_i,l_i)$ is the texture coefficient, $I(h_i,k_i,l_i)$ is the intensity from the sample being tested, $I_r(h_i,k_i,l_i)$ is the intensity from a perfectly random powder, and n is the number of peaks. Texture coefficient values are shown in Table 3.3. Texture coefficient values for a randomly oriented power have the value of 1. A texture coefficient greater than one, indicates a degree of preferred orientation for that plane. The data shows that there is some orientation to the (220) plane, but no significant change in the texture coefficients for the planes considered as $CdCl_2$ treatment time increases.

Table 3.3: Texture coefficients for CdTe layers with different treatment times.

		2 minute		4 minute		6 minute	
(hkl)	I_r	I	P_{hkl}	I	P_{hkl}	I	P_{hkl}
(111)	100	59	0.5	176	0.6	35	0.4
(220)	60	84	1.2	154	0.9	60	1.1
(311)	30	43	1.2	81	0.9	28	1.1
(400)	6	8	N/A	12	N/A	4	N/A
(331)	10	11	N/A	33	N/A	16	N/A
(422)	10	14	1.2	48	1.6	12	1.4

Lattice parameters can be found from the Nelson-Riley method [51]. Lattice parameters for each treatment time are shown in Table 3.4. These results show that there is no appreciable change in the lattice parameter due to extended $CdCl_2$ treatment.

Table 3.4: Lattice parameters for CdTe layers with different treatment times.

treatment time	lattice parameter, a (Å)
2 min	6.4862
4 min	6.4864
6 min	6.4899
ICDD	6.481

3.3 SEM Results

SEM images were taken as described in Chapter 2. Figure 3.6, Figure 3.7, and Figure 3.8 show SEM images of cells with $CdCl_2$ treatment times of 2, 4, and 6 minutes, respectively. These images show that in comparison to the 2 minute sample, the 4 and 6 minute samples do not show significant change in perceived grain size or microstructure.

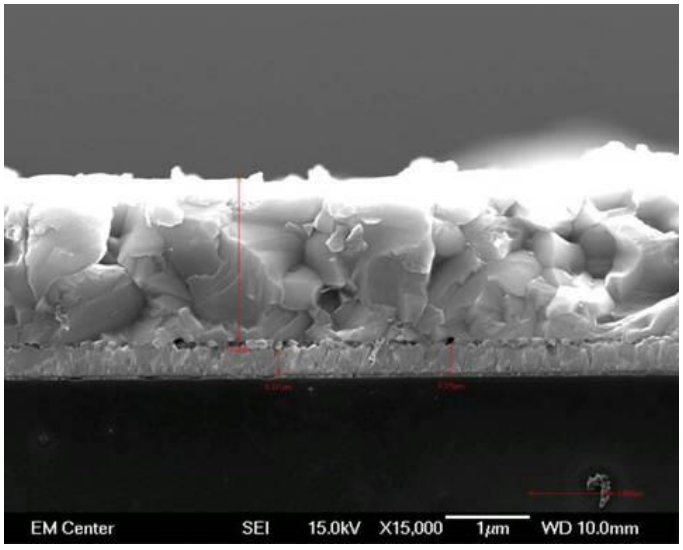

Figure 3.6: SEM image of sample with 2 minunte $CdCl_2$ treatment.

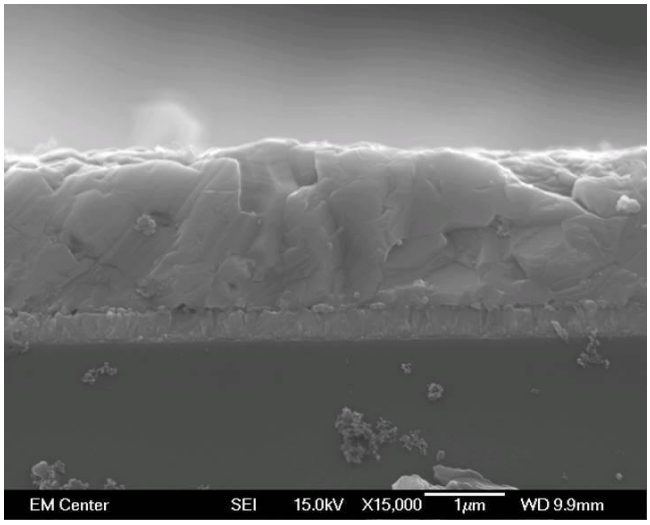

Figure 3.7: SEM image of sample with 4 minute $CdCl_2$ treatment.

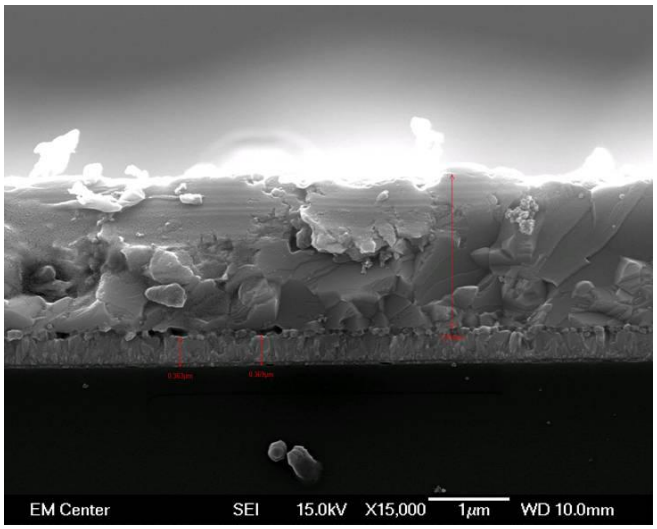

Figure 3.8: SEM image of sample with 6 minute $CdCl_2$ treatment.

3.4 AFM Results

AFM images were taken in the manner described in Chapter 2. Figure 3.9, Figure 3.10, and Figure 3.11 show AFM images of the CdTe layer surface for cells with 2, 4, and 6 minute treatment times. These images show no major differences in the apparent grain size.

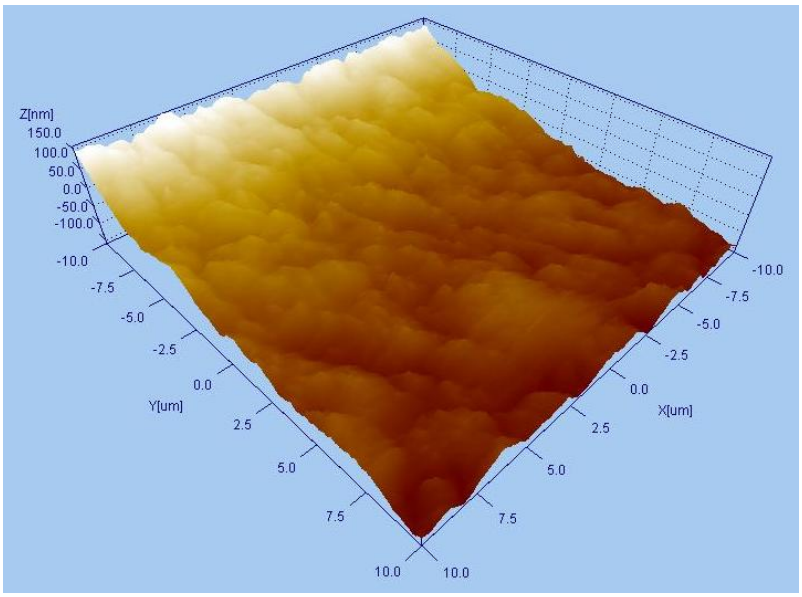

Figure 3.9: AFM image of CdTe surface of 2 min $CdCl_2$ treated sample.

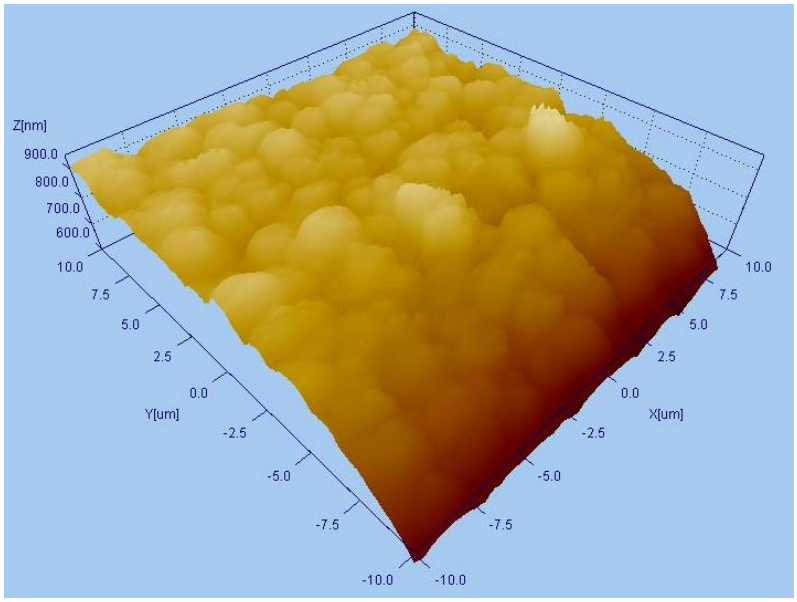

Figure 3.10: AFM image of CdTe surface of 4 min $CdCl_2$ treated sample.

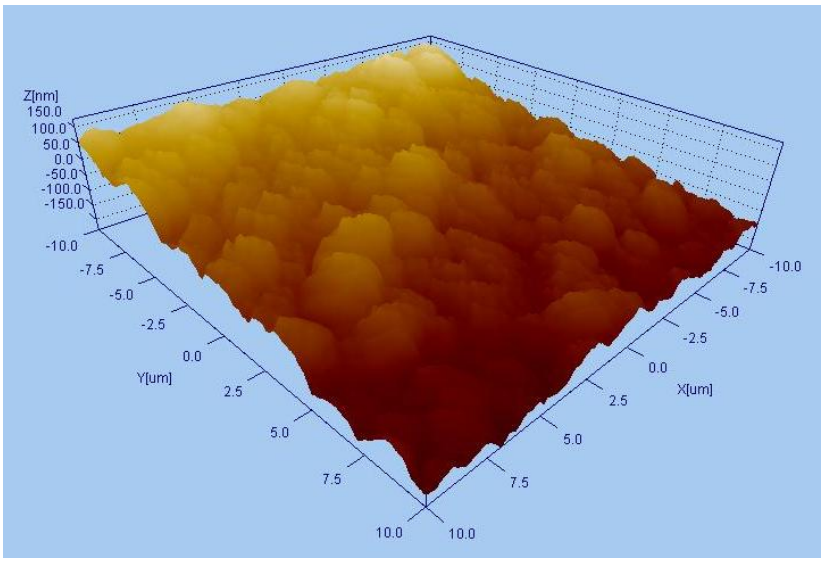

Figure 3.11: AFM image of CdTe surface of 6 min $CdCl_2$ treated sample.

3.5 J-V Results

Current-voltage measurements were done in the same manner as described in Chapter 2. The fill factor and efficiency were calculated using Equation 2-2 and Equation 2-3, respectively. Numerical results of the important solar cell parameters for this experiment are shown in Table 3.5 and graphical results of the current-voltage readings are shown in Figure 3.12.

Table 3.5: Performance data for cells with 2, 4, and 6 minute $CdCl_2$ treatment.

	η (%)	FF (%)	V_{OC} (V)	J_{SC} (mA/cm^2)
2 min $CdCl_2$	8.62	62.16	0.671	20.68
4 min $CdCl_2$	7.58	63.06	0.565	21.29
6 min $CdCl_2$	8.20	65.52	0.607	20.62

The numerical results show several trends. The open-circuit voltage and short-circuit current show opposite responses to increased treatment time. The open-circuit voltage is initially reduced as the $CdCl_2$ treatment time is decreased from 2 to 4 minutes, but increases with the 6 minute treatment. Despite this up and down response, the open-circuit voltages for the increased treatment times are both lower than the baseline 2 minute treatment. The short-circuit current increases with the lengthened treatment time from 2 to 4 minutes, but then drops to just below the value for the baseline treatment. The short-circuit current increase is fairly small compared to that of the open-circuit voltage decrease. The fill factor increases as the $CdCl_2$ treatment time is increased.

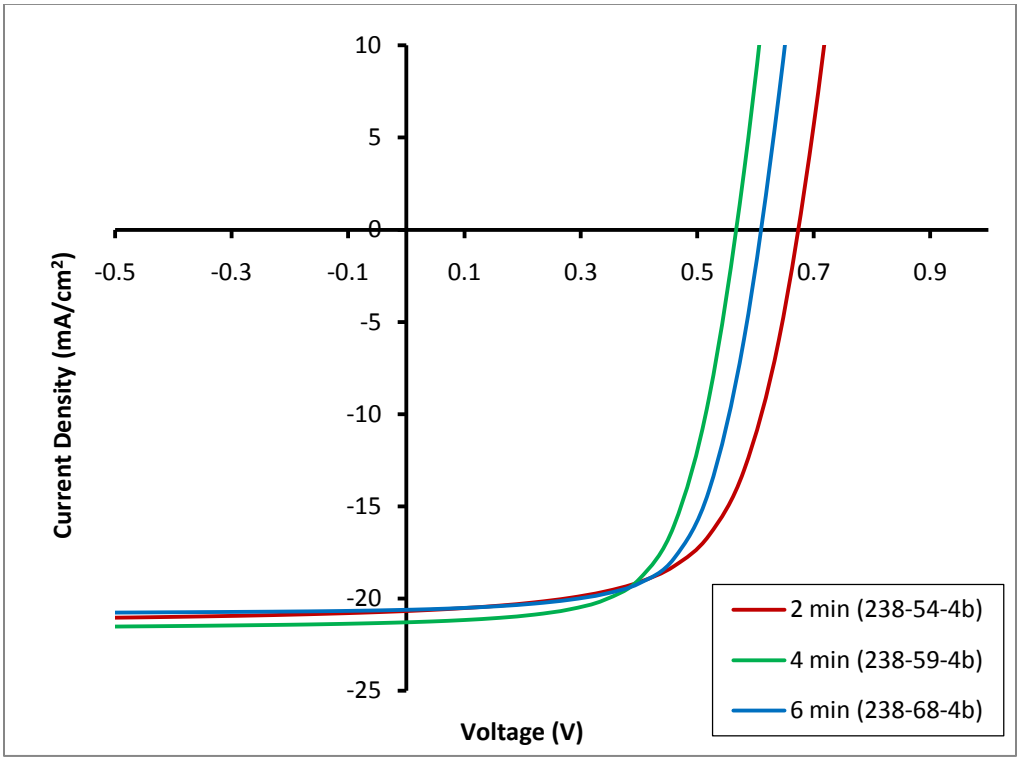

Figure 3.12: Current-voltage curves for cells with 2, 4, and 6 minutes $CdCl_2$ treatments.

All these values (FF, V_{OC}, and J_{SC}) contribute to the overall efficiency of the cell and the efficiency is the most important parameter because it dictates how much useful power can be produced of a particular cell. The efficiency drops approximately 1% as the treatment is lengthened from 2 to 4 minutes and then climbs approximately 0.5% as the treatment time is increase from 4 to 6 minutes. The overall effect of extended $CdCl_2$ treatment is reduced efficiency.

3.6 TRPL Results

Time-resolved photoluminescence measurements were conducted as discussed in Chapter 2. The PL decay curve is shown Figure 3.13. PL counts are recorded as a function of time for all samples. The PL counts create a histogram that can be taken as the PL decay curve [19]. An exponential decay curve is fit to the initial decay of the curve where the highest number of PL counts occur [38]. The tail of the decay curve can typically be omitted from curve fitting. The data shows slight biexponential decay where the PL intensity can be described by:

$$\text{PL Intensity} = C_1 \exp\left(-\frac{\tau}{\tau_1}\right) + C_2 \exp\left(-\frac{\tau}{\tau_2}\right) \tag{3-2}$$

where C_1 and C_2 are constants. The first term dominates the equation and the value of τ_1 is taken to be the value of the minority carrier lifetime. The values of the above equation for the fitted data are shown in Table 3.6. Although all the values for all samples are included in both Figure 3.13 and Table 3.6, the values of interest are those for the 2, 4, and 6 minute treatment times. The results show that for increasing $CdCl_2$ treatment times of 2, 4, and 6 minutes the lifetime values were 640 ps, 740 ps, and 769 ps, respectively.

Lifetime values are plotted as a function of $CdCl_2$ treatment time and shown in Figure 3.14.

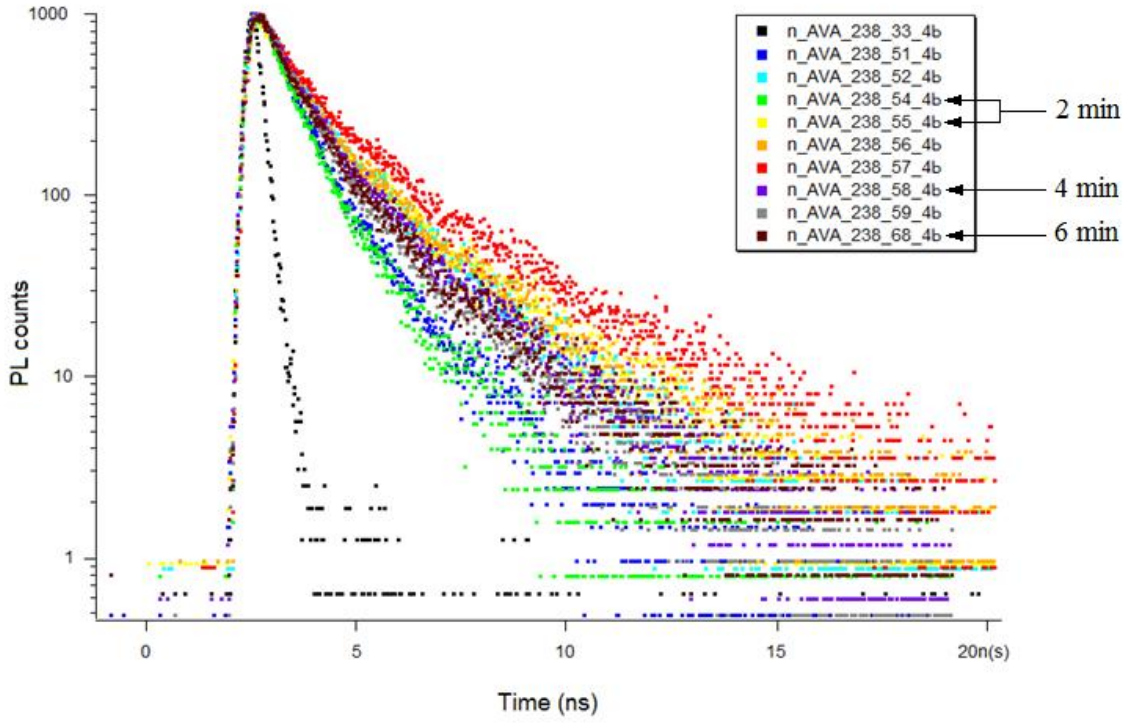

Figure 3.13: Plot of TRPL data.

Table 3.6: Curve fitting values for TRPL data.

Sample	C_1	τ_1 (ps)	C_2	τ_2 (ps)	C_2/C_1
238-51	655	**652**	169	1740	0.258
238-52	553	**841**	279	2330	0.505
238-54 (2 min)	661	**640**	155	1650	0.234
238-55 (2 min)	465	**636**	355	2190	0.763
238-56	480	**686**	346	2220	0.721
238-57	553	**842**	373	2820	0.675
238-58	572	**772**	237	2210	0.414
238-59 (4 min)	653	**740**	168	2260	0.257
238-68 (6 min)	608	**769**	195	2250	0.321

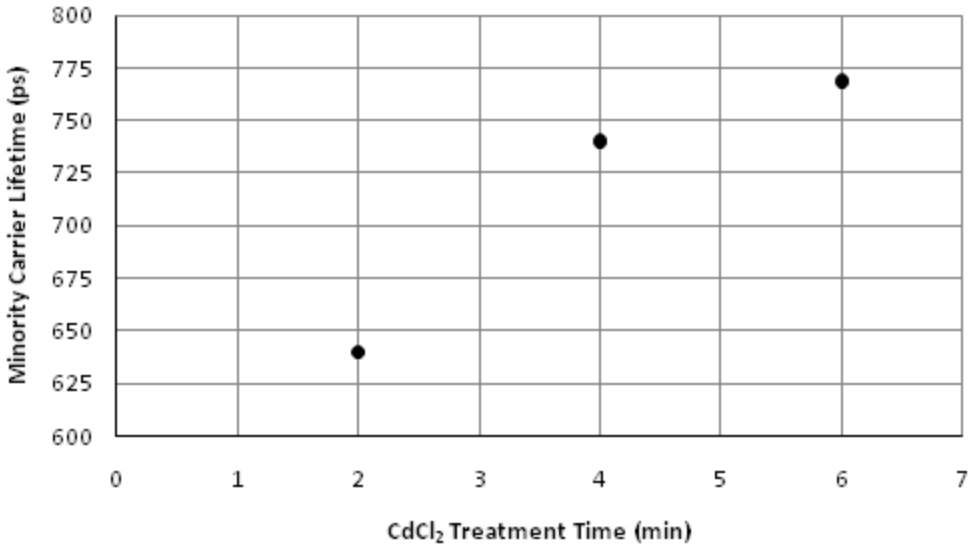

Figure 3.14: Minority carrier lifetime as a function of $CdCl_2$ treatment time.

3.7 LBIC and QE Results

Laser beam induced current and average quantum efficiency measurements were done as described in Chapter 2. LBIC and QE measurements essentially measure the same parameter but in different ways. The combination of both LBIC and QE can give a compressive summary of the photon to electron efficiency of a solar cell. LBIC images are shown in Figure 3.15, Figure 3.16, and Figure 3.17. These QE maps show some degree of non-uniformity. Each cell shows several point discontinuities below the average efficiency, but overall there is only a slight difference in uniformity as $CdCl_2$ treatment is increased.

The average cell QE values are recorded as a function of wavelength. QE curves are shown in Figure 3.18. Figure 3.18a shows the entire spectral response curve and Figure 3.18b shows an expanded view. Also highlighted for reference in the QE curves

is a vertical line corresponding to the wavelength of 638 nm, which is the wavelength of the laser used in LBIC measurements. Over the entire spectrum measured, the highest average quantum efficiency is achieved by the cell with a 4 minute treatment time. Not very much lower is the 2 minute treated cell, followed by the 6 minute treated cell. Overall, the QE curves differ less than a percent.

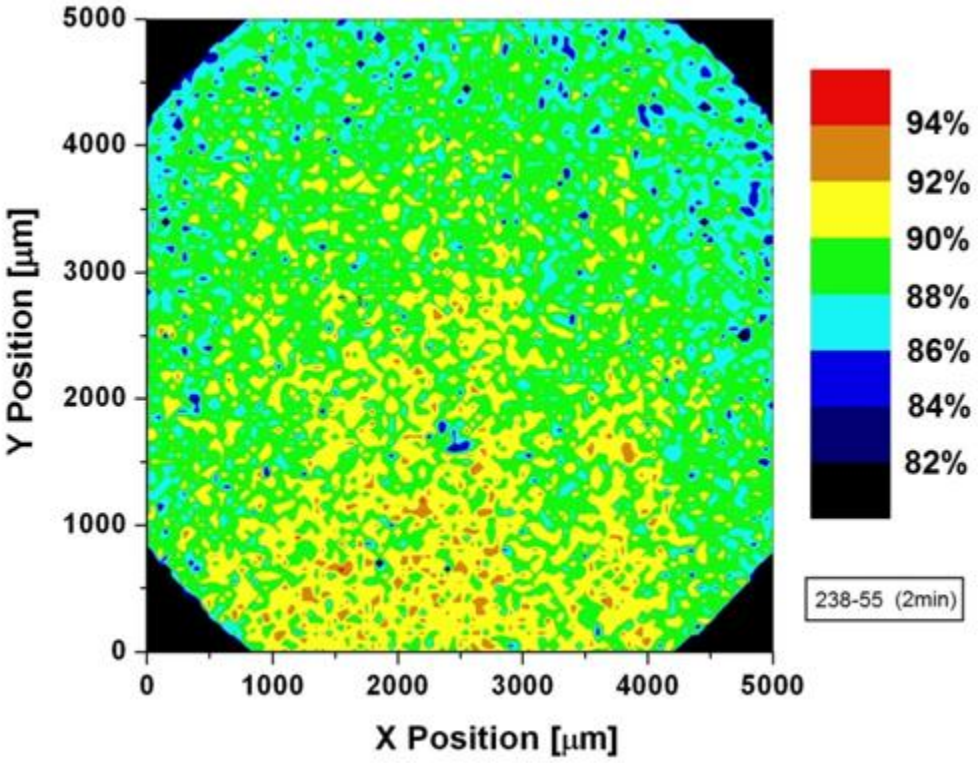

Figure 3.15: LBIC developed QE map of 2 minute $CdCl_2$ treated sample.

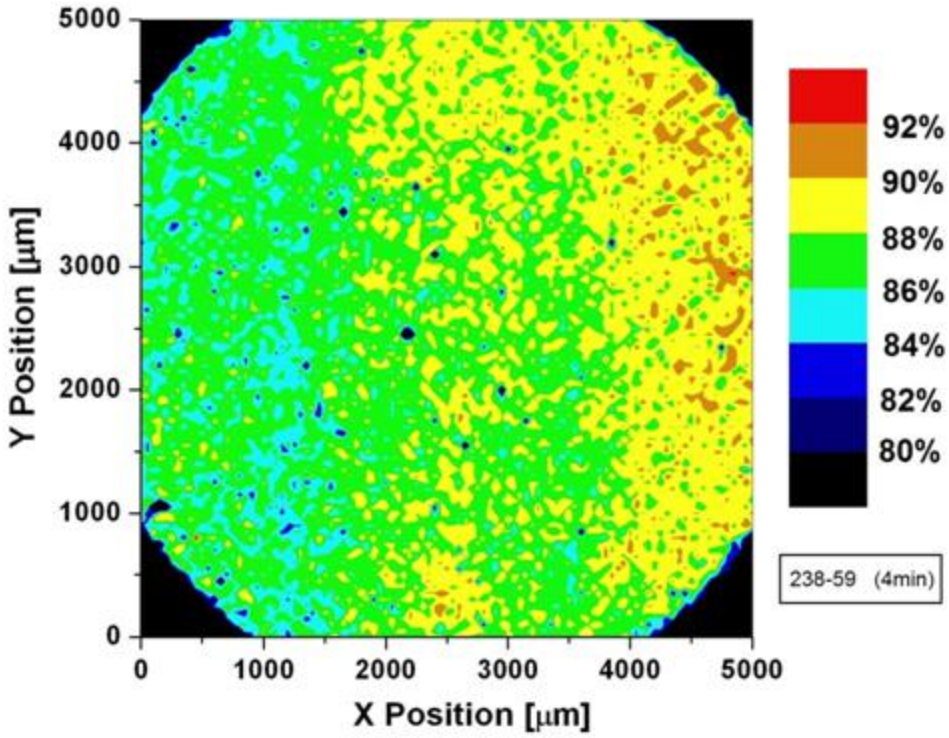

Figure 3.16: LBIC developed QE map of 4 minute $CdCl_2$ treated sample.

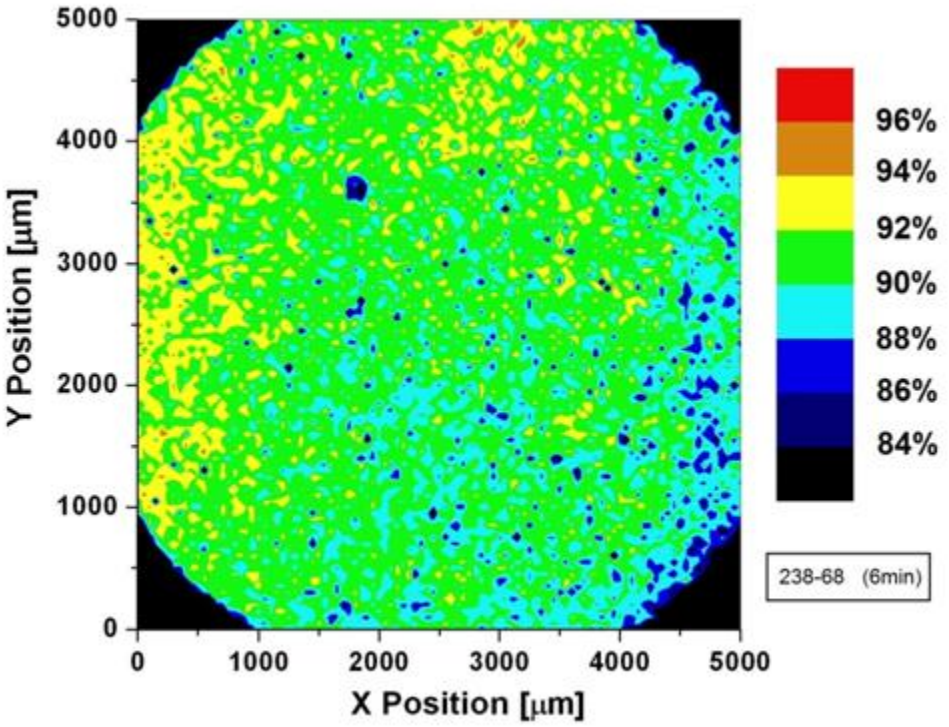

Figure 3.17: LBIC developed QE map of 6 minute $CdCl_2$ treated sample.

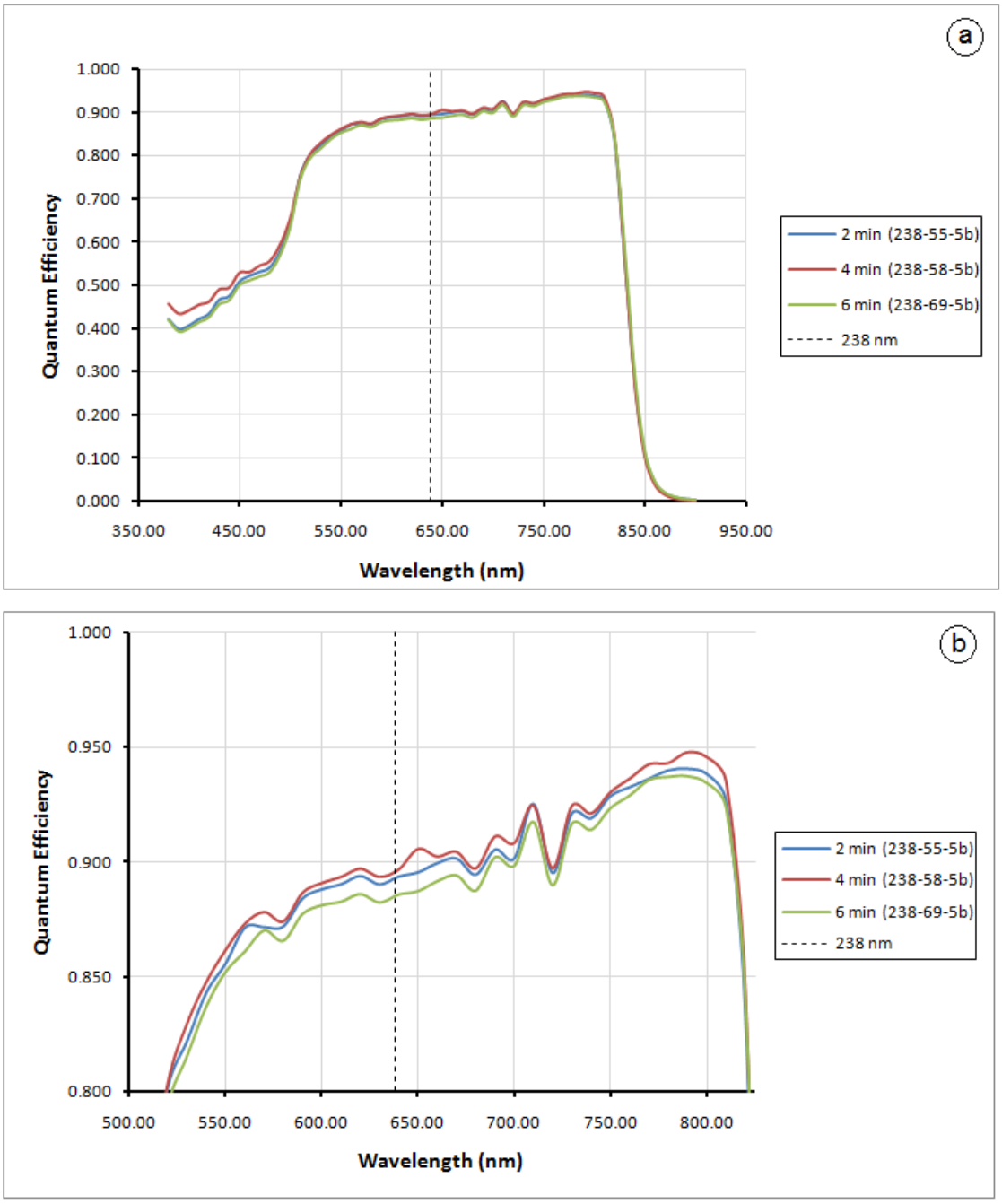

Figure 3.18: QE curves for 2, 4, and 6 minute $CdCl_2$ treatments. a) Shows the entire measure response and b) shows an expanded view of the same curves. The vertical dashed line on both graphs is a reference to response at 638 nm which is the wavelength to the laser use for LBIC measurements.

3.8 Discussion

The tests done in this study provide good insight as to the effects of the duration of $CdCl_2$ treatment on CdTe/CdS solar cells. Microstructural features were minimally affected by the $CdCl_2$ treatment, while performance was significantly impacted. Both microstructural and performance results are explained.

XRD results show that there was no appreciable change in preferred orientation or lattice parameter. Both AFM and SEM images show that there is no major recrystallization or grain growth with extended $CdCl_2$ treatments. As previously stated, $CdCl_2$ treatment can lead to grain growth and recrystallization depending on the method of depositing the CdTe layer (Table 3.1). Studies by Moutinho *et al* show that when CSS is used to deposit CdTe films, it is typical to see no recrystallization, grain growth, or significant change in microstructure due to the $CdCl_2$ treatment [29, 36, 46]. Since HPD deposition is very similar to CSS, it was expected to see similar results to those obtained with CSS.

The deposition of the CdTe layer on the CdS layer leads to lattice mismatch between the two layers. This lattice mismatch is a proponent of in-plane stress and lattice strain. The recrystallization process is directly related to the amount of lattice strain. The major cause for the lack of recrystallization and subsequent grain growth is the high temperature of the HPD process. High deposition temperatures lead to large initial grain sizes and possibly a lower concentration of defects [36, 46]. Both of these factors lead to smaller lattice strain energy and reduce the tendency for recrystallization and grain growth during the $CdCl_2$ heat treatment. It is also suggested that lattice strain energy may be further relieved by the reduction of lattice mismatch by the creation of ternary

compounds ($CdTe_xS_{x-1}$ and CdS_yTe_{1-y}) at the CdTe/CdS junction as the result of interdiffusion between the two layers [52]. The creation of a CdS_xTe_{1-x} layer resulting from sulfur was not detected by XRD. A study by Moutinho *et al* of CSS CdTe films using a similar $CdCl_2$ treatment showed that the $CdTe_{1-x}S_x$ layer was detactable by XRD only at temperatures above those used in this study [29]. Other studies by Moutinho et al show that a CdS_xTe_{1-x} was detected with PVD deposited CdTe films, but not with CSS deposited CdTe films [46]. It is suggested that the smaller grains created by PVD allow for more intragranular diffusion to create a easily detectable layer.

While the $CdCl_2$ heat treatment showed little change in the microstructure of the cells, it did have a significant impact on the device performance. It is apparent that $CdCl_2$ treatment is necessary for device quality CdTe/CdS solar cells, but the performance results obtained show that this process is quite sensitive to $CdCl_2$ deposition time. J-V results clearly show decreased performance as $CdCl_2$ treatment time is increased. The 2 minute baseline treatment yielded the best device performance. The mixed response of the solar cell parameters (Table 3.5) suggests that there may be complex competing effects at work.

Measurements of the minority carrier lifetime showed increasing values as $CdCl_2$ treatment time was increased. The primary goal of increasing the carrier lifetime is to reduce recombination of forward-bias-injected carriers and ultimately increase the open-circuit voltage [53]. Previous studies by Metzger et al [38] have shown that there is a strong correlation between carrier lifetime and open-circuit voltage. Figure 3.19 shows a plot of open-circuit voltage as a function of lifetime. There is a clear trend that as lifetime increases the open-circuit voltage increases as well. This combined with the

result of increased lifetime with increased $CdCl_2$ treatment time suggests that increasing $CdCl_2$ treatment time would increase the open-circuit voltage in this study. However, this was not the case. Experimental results showed that extended $CdCl_2$ treatment reduced the open-circuit voltage. While this result is not what was expected, it is not unreasonable. Open-circuit voltage is controlled by numerous variables. These variables include shunt resistance, series resistance, interface charge and recombination, grain boundary charge and recombination, defects, recombination within the grains, S and Te interdiffusion, CdS thickness, and others. Since all these variables are closely interconnected, it is virtually impossible to change one and not affect the others.

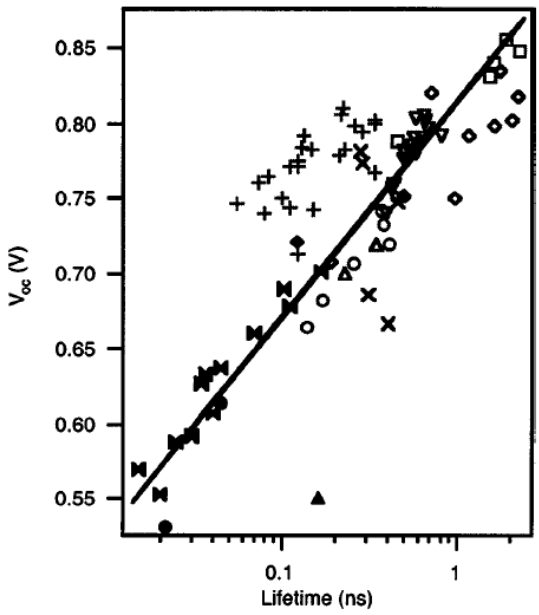

Figure 3.19: Relationship of open-circuit voltage and minority carrier lifetime for CdTe cells. Data points that are solid represent cells with no $CdCl_2$ treatment. Image taken from ref [38].

Sulfur diffusion plays a major role in final device performance as well as affects many of the previously mentioned variables contributing to open-circuit voltage. Sulfur

diffuses from the CdS layer occurs primarily during the $CdCl_2$ treatment. Figure 3.1 clearly shows sulfur diffusion at the junction of CdTe films with $CdCl_2$ treatments done by Metzger *et al* that are similar to those carried out in this study [8]. As mentioned previously, this interdiffusion produces a $CdTe_{1-x}S_x$ alloy at the junction. This alloying at the junction can lead to the formation of a reduced band gap layer that is possible reason for reduced device performance [31, 32]. If the sulfur content varies throughout the thickness, and sulfur has strong effects on device properties, such as carrier lifetime, then these properties vary through the thickness as a function of sulfur content.

A similar study was done at CSU to determine the effects of increased $CdCl_2$ deposition time (Table 3. 7). The $CdCl_2$ deposition was varied in the same way as in this study but other process parameters were different. These results show slightly higher performance values, but the overall trend of decreased performance with in increased $CdCl_2$ treatment is similar.

Table 3. 7: J-V results from a similar study done by at CSU.

	η (%)	FF (%)	V_{OC} (V)	J_{SC} (mA/cm^2)
2 min $CdCl_2$	12.3	71.7	0.783	21.9
4 min $CdCl_2$	9.4	65.2	0.614	23.4
6 min $CdCl_2$	7.3	57.1	0.566	22.4

Potter et al has also shown decreased CdTe device performance with increasing $CdCl_2$ annealing [31]. These results are displayed in Table 3.8 and show that there is an initial increase in device performance from no treatment to a ten minute anneal, but as treatment time increases, device performance, including the open-circuit voltage, decreases. Potter et al suggest that a possible reason for reduced performance with

increased annealing is the formation of low bandgap $CdTe_{1-x}S_x$ layer resulting from S diffusion from the CdS layer.

Table 3.8: Device performance values with increased $CdCl_2$ anneal time [31].

Anneal time (min)	V_{OC} (V)	J_{SC} (mA/cm^2)	FF (%)	η (%)
as grown	0.55	13	31	2.1
10	0.70	22	57	8.4
20	0.72	21	51	7.9
30	0.67	18	53	6.6
40	0.64	20	53	6.7
60	0.62	19	50	6.0

The amount of sulfur diffusion and content is a key to improving lifetime and has strong effects in many other areas of the device performance. The source of sulfur that diffuses into the CdTe has been shown to come only from the CdS layer and not from other material impurities [11]. Sulfur diffusion and subsequent $CdTe_{1-x}S_x$ formation at the junction also leads to thinning of the CdS layer [32, 52]. Sulfur diffusion likely occurs along grain boundaries [7, 8, 38] which means that CdS thinning could be non-uniform. Thinning of the CdS layer can produce a weak diode and can lead to reduced open-circuit voltage as shown in Figure 3.20. The curves in Figure 3.20 show very similar trends to J-V data for this study. As the CdS layer is thinned, the short-circuit current increases but the open-circuit voltage decreases. This could also be a reason for reduced performance.

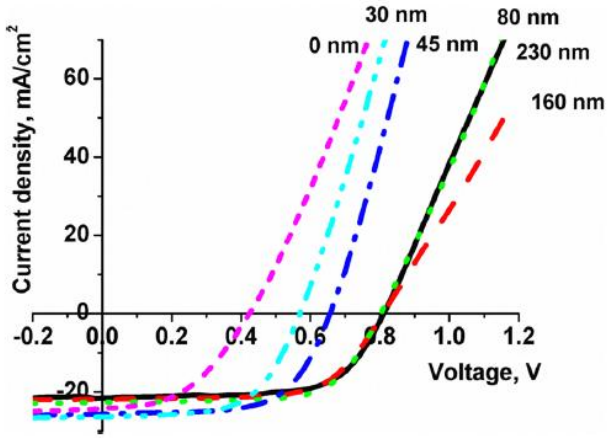

Figure 3.20: J-V curves for CdTe solar cells with different CdS layer thicknesses. Image taken from ref [54].

Quantum efficiency results show some differences with $CdCl_2$ treatment time as well. While there is some inconsistency between the 2 and 4 minute treatments, the 6 minute treatment shows a decrease in performance. Values of short-circuit current appear to scale with the average QE values. The 4 minute treatment has the best overall spectral response and as a result the best short-circuit current value. All three treatments show an increase in QE with increased wavelength. Alloying at the junction and bandgap reduction can lead to higher long wavelength QE values, which are seen in this study [7]. There are many factors that can hinder photon penetration and absorption by the CdTe layer. Figure 3.21 shows various QE loss mechanisms that affect CdTe solar cells.

LBIC images show the uniformity of the QE response (Figure 3.15, Figure 3.16, Figure 3.17). The several point defects that are visible may be the result of inclusions produced during cell fabrication [55]. All three treatment times show some degree of nonuniformity. This could be the result of non-uniform diffusion of sulfur from the CdS layer which is aided by the $CdCl_2$ treatment [48]. The non-uniform diffusion of sulfur from the CdS layer leads to a non-uniform thickness of the CdS layer. CdS thinning can

lead to better photon transmission to the CdTe layer, but excessive thinning leads to non-uniform diode quality, reduced photocurrent, and shunting.

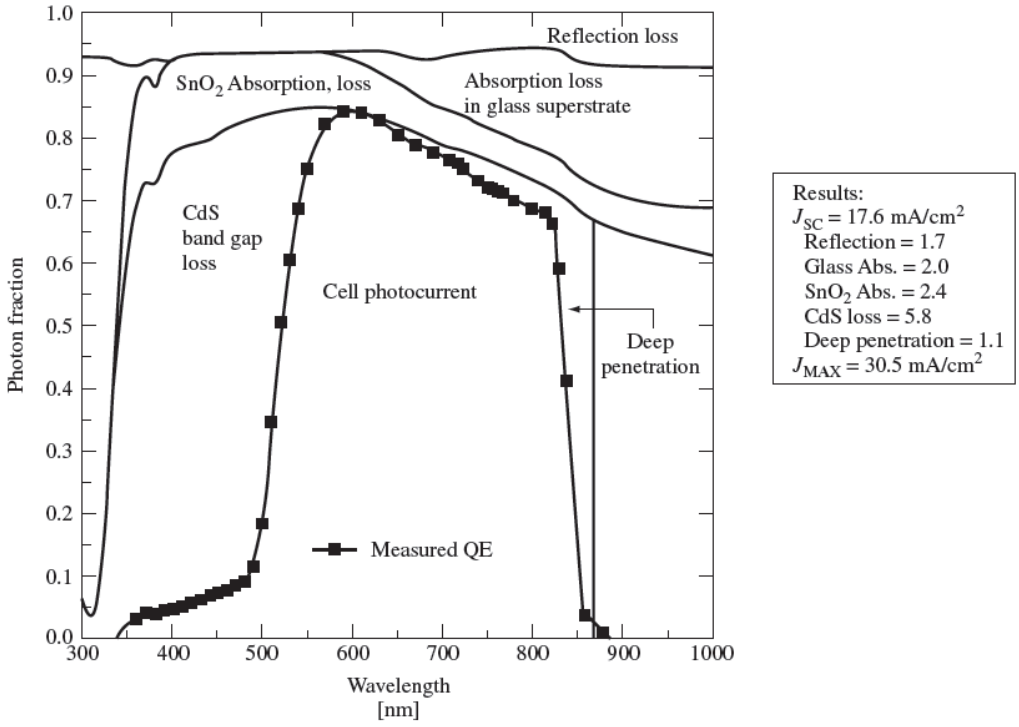

Figure 3.21: Graph of QE versus wavelength showing different photon losses. This particular CdTe cell suffered considerably from losses but provides a good example of the different loss mechanisms. Image taken from ref [7].

3.9 Conclusion

Extended $CdCl_2$ treatment had little effect on the microstructural properties of the solar cells in this study. This was due to the method of CdTe deposition. The high deposition temperatures used in HPD allow for large grains to form with low lattice strain energy which essentially prevents recrystallization and further grain growth.

Extended $CdCl_2$ treatment did have a significant effect on the performance of the solar cells in this study. Lengthening the $CdCl_2$ treatment beyond the 2 minute baseline treatment had mixed effects on the major solar cell parameters (V_{OC}, J_{SC}, FF, η), but the

overall effect was negative. Minority carrier lifetime values increased with $CdCl_2$ treatment time increased while open-circuit voltage and overall efficiency decreased. An explanation for this decreased performance is thinning of the CdS layer by diffusion of sulfur into the CdTe layer and the formation of a lower bandgap $CdTe_{1-x}S_x$ alloy at the junction. Similar to other studies, a $CdTe_{1-x}S_x$ was not detected with XRD, despite the fact that sulfur diffusion is shown to occur during the $CdCl_2$ treatment. While, a moderate amount of CdS thinning can increase photon transmission, an excessive amount leads to poor diode properties. The LBIC images suggest a small degree of non-uniform photocurrent production which supports non-uniform sulfur diffusion and CdS thinning.

In order to better understand the mechanisms at work, further study with a larger number of samples and shorter treatment time increments is recommended. It is clear that the extended $CdCl_2$ treatment in this study decreased overall cell performance and the baseline 2 minute treatment yielded the best performance. In order to better understand the mechanisms effecting device performance and attempt to verify assumption made, solar cell modeling was employed.

CHAPTER 4: Modeling CdTe/CdS Solar Cells

4.1 Introduction

In the past several decades, numerical modeling has become a necessary tool for scientists and engineers. The ability to model complex problems gives the freedom to explore different scenarios without doing costly experiments or building expensive prototypes. Numerical modeling of photovoltaic devices is a very useful tool for investigating issues related to solar cell structure and performance. Some of the necessary capabilities of a solar cell modeling program are listed in Table 4.1.

Table 4.1: Various issues that a solar cell simulation program should address [56].

▪ Multiple layers
▪ Band discontinuities in E_C and E_V: ΔE_C and ΔE_V
▪ Large bandgaps: $E_g > 2$ - 3.7 eV
▪ Graded bandgaps: $E_g(x)$ and also $\chi(x)$, $N_C(x)$, $N_V(X)$, $\alpha(X)$,…
▪ Recombination and charge in deep bulk states
▪ Recombination and charge in deep interface states
▪ Simulation of non-routine measurements: J-V, C-V, C-f, QE(λ),…all as a funcion of Temperature
▪ Fast and easy to use

Modeling in this study was performed using AMPS (**A**nalysis of **M**icroelectronic and **P**hontonic **S**tructure) [57] and SCAPS (**S**olar cell **CAP**acitence **S**imulator) [58]. Both of these programs are intended for one dimensional modeling of multi-layered solar cell devices. AMPS was developed by Stephen Fonash of Pennsylvania State University. It allows for up to 30 independent layers to be modeled. It solves problems by dividing the device into grid points and simultaneously solving the steady state semiconductor equations at each grid point [59]. It is a fairly simple program to use and allows for multiple problems to be worked simultaneously. It is also possible to simulate graded layers in AMPS, but it involves incrementally changing material properties over a number of separate layers. Some of the drawbacks of this program are that grid sizes are somewhat limited, which can hinder modeling devices with a large number of layers and it takes relatively long time to solve problems compared to similar programs. SCAPS was developed by Marc Burgelman at the University of Gent. It was primarily designed for modeling CdTe and CIGS devices. It allows for up to 7 layers to be modeled with interface properties between each layer and it allows for graded layer properties to be used.

The primary reasons for modeling solar cells are investigating the feasibility of suggested physical explanations of cell performance, predicting the effect of changes in material properties and geometry on cell performance, and correlating modeling results to experimental results [60]. One of the difficulties of modeling solar cells is producing an initial model as starting point for further investigation. Fortunately, a set of baseline parameters for modeling CdTe solar cells has been developed [60]. The baseline parameters used for this study can be seen in Appendix A. The strategy of modeling is to

fix a set of accepted device parameters and then begin to vary and investigate the effects of other parameters separately. This strategy was used in this study. Modeling was done to investigate the experimental data that was presented in Chapter 3. The goal for each model was to gain more understanding of the mechanisms that effect performance by isolating the effects of specific device parameters and not necessarily attempting to exactly match the measured results. Since there are a fairly large number of variables and resulting device scenarios, those that readily apply to the experimental data were investigated. The variables that are investigated in this modeling study are minority carrier lifetime, CdS layer thickness, and the role of a low bandgap CdTe layer.

4.2 Modeling Results

The results from Chapter 3 show that even though minority carrier lifetime values increased overall device performance decreased. Modeling was used to better understand how and to what degree increased minority carrier lifetimes effect performance. The role of minority carrier lifetime with respect to device performance was also modeled in two parts. The first was simulating a large range of lifetime values, ranging from 0.001 ns to 1000 ns. This was done to get a broad picture of how lifetime values affect device performance. The baseline model was used and only lifetime values were changed. Numerical performance values are shown in Table 4.2 and current-voltage curves are shown in Figure 4.1. As expected, these results clearly show that as lifetime is increased performance increases. The largest performance gains are seen as the lifetime is increased from 0.001 ns to 1 ns. Above 1 ns the performance still increases but appears

to reach a maximum. When the lifetime is increased from 100 ns to 1000 ns there is virtually no change in performance.

Table 4.2: Performance values for large range of minority carrier lifetime values.

τ (ns)	V_{OC} (V)	J_{SC} (mA/cm^2)	FF (%)	η (%)
0.001	0.451	1.514	38.5	0.239
0.01	0.578	7.532	42.3	1.676
0.1	0.698	16.546	51.9	5.458
1	0.814	20.704	70.4	10.781
10	0.882	21.28	78.8	13.448
100	0.894	21.339	82.1	14.242
1000	0.895	21.345	82.6	14.351

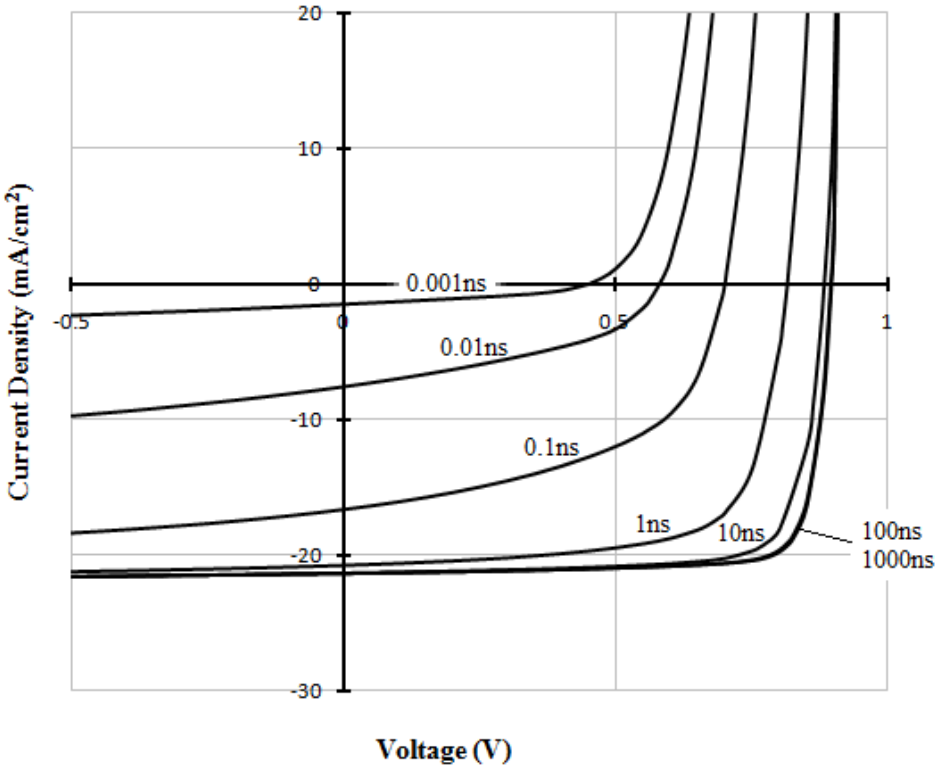

Figure 4.1: Current-voltage curves for a large range of minority carrier lifetime values. The curves for 100 ns and 1000 ns are labeled together because there is essentially no difference between them.

Another set of models was done for lifetime values equal to those measured in Chapter 3 to show to what degree performance would increase if only lifetime was improved. Numerical performance values are shown in Table 4.3 and current-voltage curves are shown in Figure 4.2. Just as in previous set of models with a wide range of lifetimes, performance increased with increasing lifetimes, but this time on a smaller scale.

Table 4.3: Performance values for measured minority carrier lifetimes.

τ (ns)	V_{OC} (V)	J_{SC} (mA/cm^2)	FF (%)	η (%)
0.640	0.794	20.364	67.6	9.934
0.740	0.8	20.49	68.6	10.224
0.769	0.802	20.521	68.8	10.298

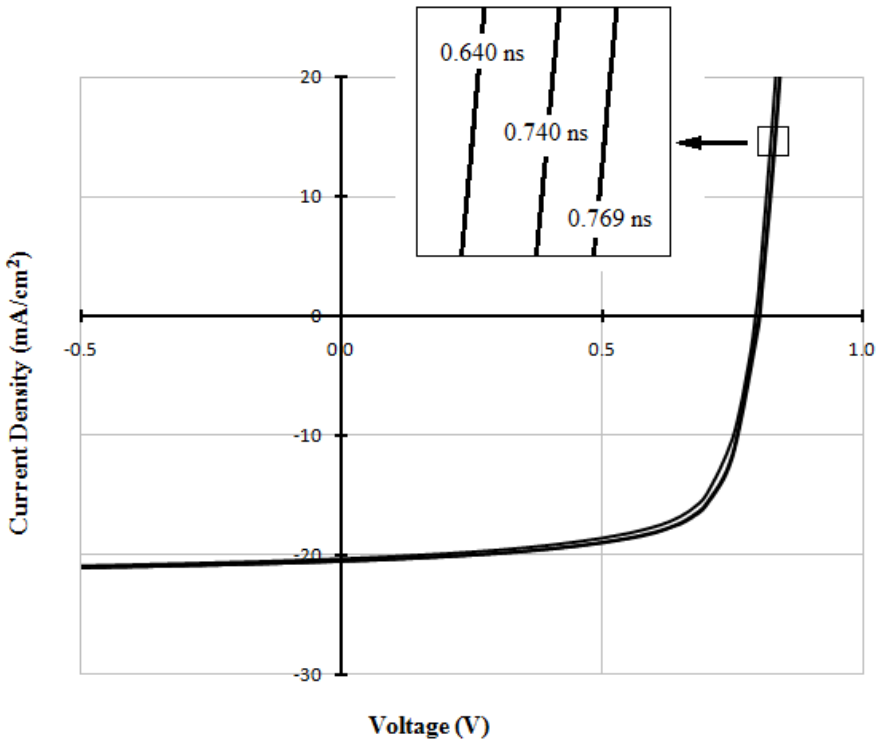

Figure 4.2: Current-voltage curves for measured minority carrier lifetimes.

In Chapter 3 it is also suggested that a possible reason for performance change was related to thinning of the CdS layer due to sulfur diffusion and the creation of a low bandgap CdTe layer. The effect of the CdS layer thinning alone was first investigated. The baseline model was run with a range of CdS layer thicknesses ranging from 0.05µm to 0.25µm. Numerical values for each thickness are shown Table 4.4 and current-voltage curves are shown Figure 4.3. These results clearly show an increase in performance as the CdS layer thickness decreases. Open-circuit voltage is nearly constant while the short-circuit current steadily increases as the thickness decreases.

Table 4.4: Performance values for varied CdS thickness models.

CdS thickness (µm)	V_{OC} (V)	J_{SC} (mA/cm^2)	FF (%)	η (%)
0.05	0.7955	22.65	79.30	14.29
0.10	0.7933	21.29	79.18	13.37
0.15	0.7918	20.40	79.10	12.78
0.20	0.7907	19.81	79.04	12.38
0.25	0.7900	19.40	79.00	12.11

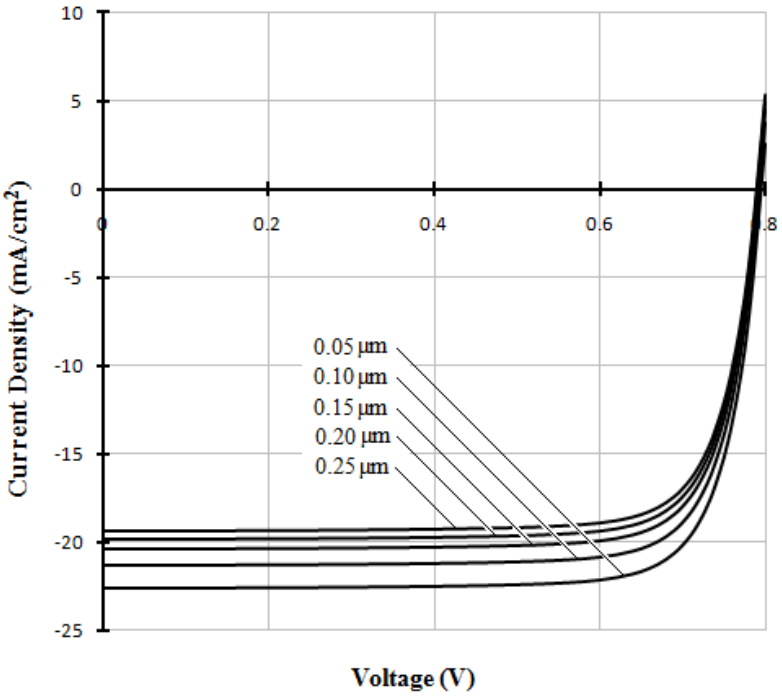

Figure 4.3: Current-voltage curves for varied CdS thickness models.

Models were then made simulate the formation of a lower bandgap CdTe layer resulting from sulfur diffusion from the CdS layer. Figure 4.4 shows the change in bandgap of CdTe as sulfur content is increased. The value of the lower bandgap that is used is 1.4 eV, which corresponds to $CdTe_{0.75}S_{0.25}$ [31, 61]. The bulk CdTe layer remains at the baseline value of 1.5 eV.

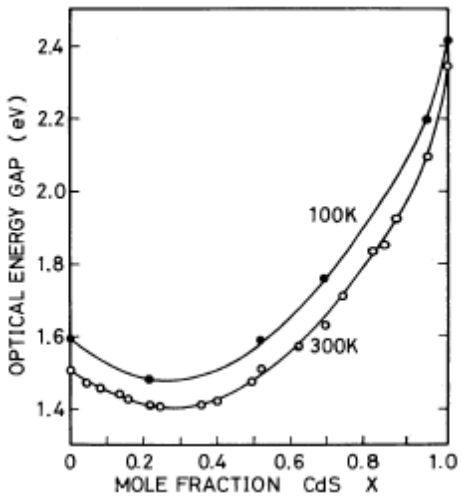

Figure 4.4: Bandgap change of $CdTe_{1-x}S_x$ based on sulfur content. Image taken from ref [61].

The different device structures that were modeled are shown in Figure 4.5. They are made to represent the formation and continued growth of a low bandgap CdTe layer as $CdCl_2$ treatment is increased. Table 4.5 shows performance data for models with different thickness of the low bandgap CdTe layer and J-V curves are shown in Figure 4.6. These results show that overall performance is steadily reduced as a result of the introduction and growth of a low bandgap CdTe layer. Figure 4.7 shows both J_{SC} and V_{OC} as functions of the low bandgap CdTe layer thickness. The V_{OC} steadily decreases while the J_{SC} decreases and then begins to increase.

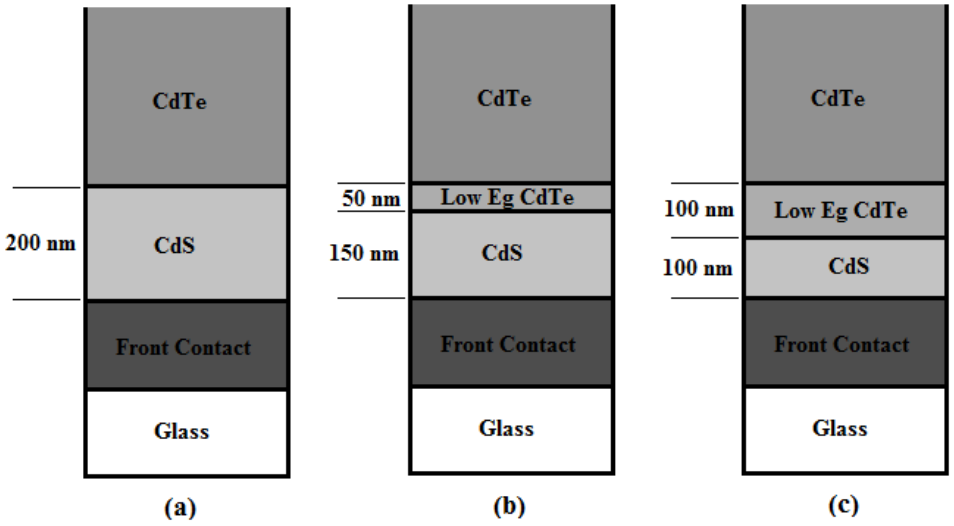

Figure 4.5: Thicknesses of CdS and low bandgap CdTe layers. (a) baseline case, (b) represents the formation of the low bandgap CdTe layer, and (c) represents the growth of the low bandgap CdTe layer with increasing $CdCl_2$ treatment. Not to scale.

Table 4.5: Performance values for different thicknesses of the low bandgap CdTe layer.

CdS thickness (nm)	low bandgap CdTe layer (nm)	V_{OC} (V)	J_{SC} (mA/cm^2)	FF (%)	η (%)
200	0	0.782	20.108	65.8	9.410
175	25	0.773	18.519	64.1	8.345
150	50	0.764	17.873	62.2	7.731
125	75	0.752	18.689	56.7	7.248
100	100	0.737	20.356	52.0	7.087

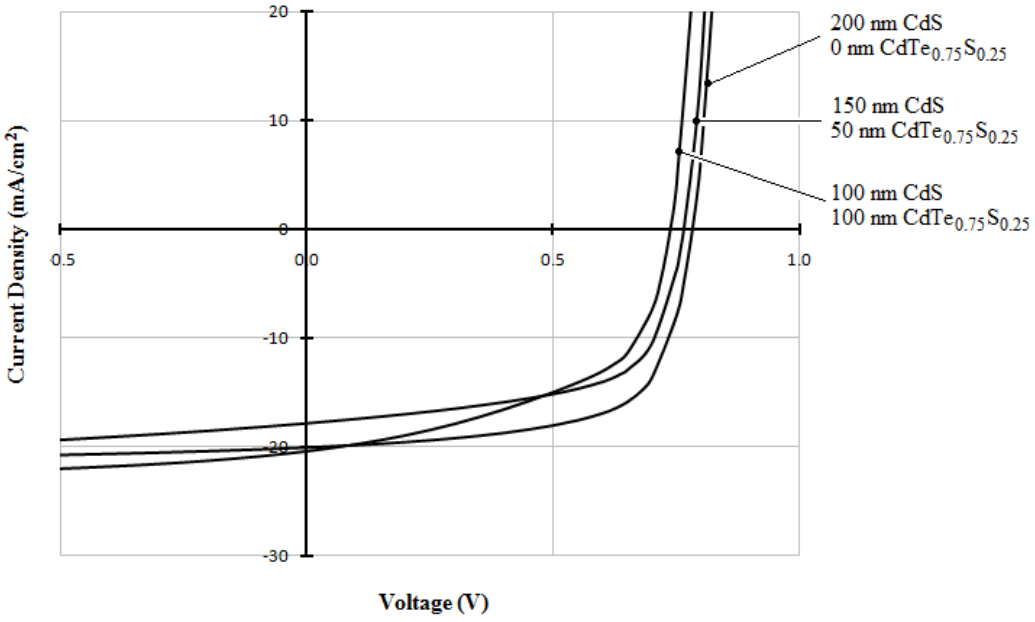

Figure 4.6: Current-voltage curves for different thicknesses of the low bandgap CdTe layer.

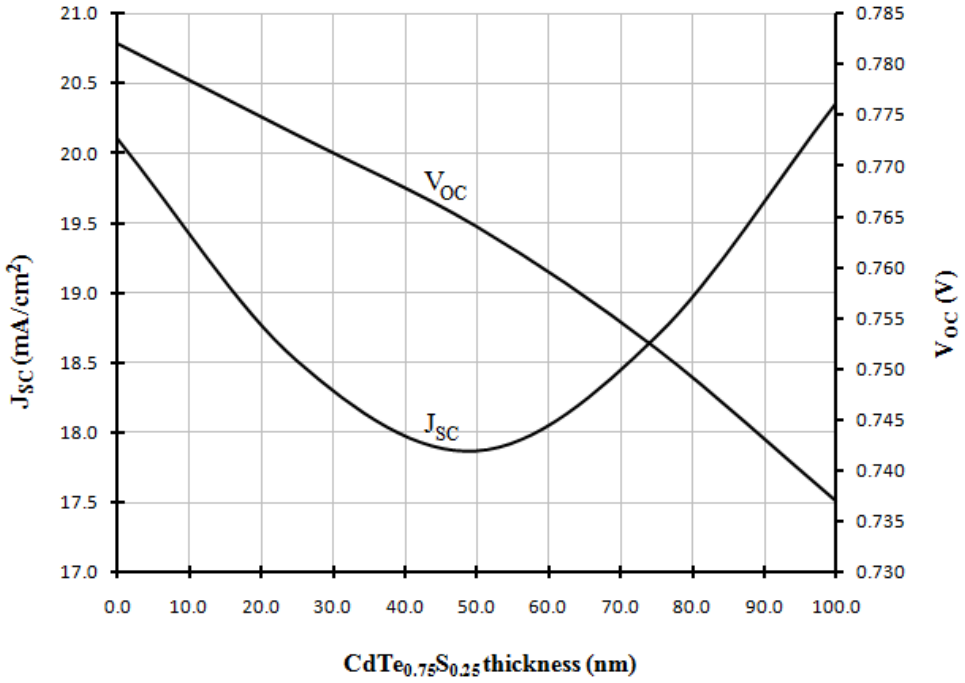

Figure 4.7: Changes in V_{OC} and J_{SC} with different thicknesses of the low bandgap CdTe layer.

4.3 Discussion

The experimental results recorded and discussed in Chapter 3 show several trends that were investigated with modeling. As $CdCl_2$ treatment time is increased, minority carrier lifetime increased while overall performance decreased. It was also suggested that extending the $CdCl_2$ treatment time leads to excess sulfur diffusion which promotes thinning of the CdS layer and formation of a low bandgap CdTe layer. To investigate these trends and hypotheses, each was investigated separately to understand the individual effects.

The effects of increased lifetime values alone were very clear and not surprising. Models did show that in range of lifetime values seen experimentally, the benefits of increased lifetime are somewhat small. If performance is to be significantly increased, the increase in lifetime values would need to higher. This means that positive effects of increased lifetime can easily be outweighed by other detrimental effects.

Another set of simulations were done to model the formation and growth of a low bandgap CdTe layer resulting from sulfur diffusion and thinning of the CdS layer. Thinning of the CdS layer alone, showed that J_{SC} was steadily increased as the CdS layer is thinned. It must be noted that the model assumes a perfectly uniform CdS layer. In the actuallity, the CdS layer is not perfectly uniform. Therefore, the model will continue to show increased J_{SC} to very thin CdS layers, while in an actual solar cell, layers this thin would be subject to shunting and poor diode quality.

When the low bandgap CdTe layer was added, the results showed that as the layer formed and increased, overall performance decreased. All of the solar cell parameters steadily decreased, except the J_{SC}. The J_{SC} values decreased until the low

bandgag CdTe layer reached about 50 nm and then began to increase. It is important to keep in mind that as the low bandgap CdTe layer is growing the CdS layer is being thinned. It seems that there is balance between negative effect of the increased low bandgap CdTe layer and the positive effects of the thinning of the CdS layer. This model behavior is similar to the measured values of J_{SC}, where the values rise and fall with extended $CdCl_2$ treatment. These modeling results support the assumption of the formation of low bandgap CdTe layer a reason for decreased performance with increasing levels of $CdCl_2$ treatment.

4.4 Conclusion

The aim of the modeling done in this study was not to exactly replicate the experimental results, but to further investigate the validity of the assumptions for decreased performance in Chapter 3. Modeling the effects of changing material properties separately helps to differentiate the effects. It was shown that increasing lifetime alone raises solar cell performance, but also that the benefits of the lifetime increases of those measured are small in comparison to other detrimental effects. Thinning of the CdS layer thickness also increases device performance primarily with elevated short-circuit current values, but perfectly modeled CdS layers may not represent real world effects. The effect of a low bandgap CdTe layer formation and growth is reduced overall performance.

REFERENCES

[1] "Key World Energy Statistics," International Energy Agency, Paris2009.

[2] M. Kaltschmitt, *et al.*, *Renewable energy technology, economics, and environment*. Berlin ;: Springer, 2007.

[3] R. L. Evans, *Fueling our future an introduction to sustainable energy*. Cambridge ;: Cambridge University Press, 2007.

[4] J. R. Hook and H. E. Hall, *Solid State Physics, 2nd Edition*: Wiley, 1995.

[5] J. L. Gray, "The Physics of the Solar Cell," in *Handbook of Photovoltaic Science and Engineering*, S. H. Antonio Luque, Ed., ed, 2004, pp. 61-112.

[6] W. Shockley and J. W. T. Read, "Statistics of recombinations of holes and electrons," *Physical Review*, vol. 87, pp. 823-842, 1952.

[7] B. E. McCandless and J. R. Sites, "Cadmium Telluride Solar Cells," in *Handbook of Photovoltaic Science and Engineering*, S. H. Antonio Luque, Ed., ed, 2004, pp. 617-662.

[8] W. K. Metzger, *et al.*, "CdCl2 treatment, S diffusion, and recombination in polycrystalline CdTe," *Journal of Applied Physics*, vol. 99, 2006.

[9] X. Wu, "High-efficiency polycrystalline CdTe thin-film solar cells," *Solar Energy*, vol. 77, pp. 803-814, 2004.

[10] "Best Research Cell Efficiencies," ed: National Renewable Energy Laboratory, 2004.

[11] M. Emziane, *et al.*, "Effect of the purity of CdTe starting material on the impurity profile in CdTe/CdS solar cell structures," 2005, pp. 1327-1331.

[12] K. Zweibel and V. Fthenakis, "Cadmium Facts and Handy Comparisons," ed: National Renewable Energy Laboratory and Brookhaven National Laboratory.

[13] V. M. Fthenakis and H. C. Kim, "CdTe photovoltaics: Life cycle environmental profile and comparisons," *Thin Solid Films*, vol. 515, pp. 5961-5963, 2007.

[14] K. L. Barth, "Abound solar's CdTe module manufacturing and product introduction," in *2009 34th IEEE Photovoltaic Specialists Conference, PVSC 2009, June 7, 2009 - June 12, 2009*, Philadelphia, PA, United states, 2009, pp. 002264-002268.

[15] K. L. Barth, *et al.*, "Apparatus and Process for the Mass Production of Photovoltaic Modules," USA Patent, 2002.

[16] K. L. Barth, *et al.*, "Advances in continuous, in-line processing of stable CdS/CdTe devices," in *29th IEEE Photovoltaic Specialists Conference, May 19, 2002 - May 24, 2002*, New Orleans, LA, United states, 2002, pp. 551-554.

[17] K. L. Barth, *et al.*, "Consistent processing and long term stability of CdTe devices," in *31st IEEE Photovoltaic Specialists Conference - 2005, January 3, 2005 - January 7, 2005*, Lake Buena Vista, FL, United states, 2005, pp. 323-326.

[18] D. Bonnet, "Manufacturing of CSS CdTe solar cells," *Thin Solid Films*, vol. 361, pp. 547-552, 2000.

[19] K. Durose, *et al.*, "Physical characterization of thin-film solar cells," *Progress in Photovoltaics: Research and Applications*, vol. 12, pp. 177-217, 2004.

[20] P. A.-. Tipler and R. A. Llewellyn, *Modern physics*, 4th ed. ed. New York: W.H. Freeman, 2002.

[21] K. Li, *et al.*, "Microstructural study on the surface and interface of CdTe/CdS solar cells," *Journal of Materials Science: Materials in Electronics,* vol. 8, pp. 125-132, 1997.
[22] D. K. Schroder, *Semiconductor material and device characterization,* 3rd ed. ed. [Piscataway, NJ]: IEEE Press Wiley, 2006.
[23] W. R. Bowen and N. Hilal, *Atomic force microscopy in process engineering an introduction to AFM for improved processes and products,* 1st ed. ed. Burlington, Mass.: Butterworth-Heinemann, 2009.
[24] D. Phillips, *et al.*, "Time-Correlated Single Photon Counting," *Analytical Instrumentation,* vol. 14, pp. 267-292, 1985.
[25] W. K. Metzger, *et al.*, "Characterizing recombination in CdTe solar cells with time-resolved photoluminescence," in *2006 IEEE 4th World Conference on Photovoltaic Energy Conversion, WCPEC-4, May 7, 2006 - May 12, 2006,* Waikoloa, HI, United states, 2007, pp. 372-375.
[26] G. D. Gilliland, "Photoluminescence spectroscopy of crystalline semiconductors," *Materials Science and Engineering R: Reports,* vol. 18, pp. 99-400, 1997.
[27] *CSU Photovoltaics Laboratory (http://www.physics.colostate.edu/groups/photovoltaic/)*.
[28] J. Hiltner, "Investigation of Spatial Variations in Collection Efficiency of Solar Cells," Doctor of Philosophy, Department of Physics, Colorado State University, Fort Collins, 2001.
[29] H. R. Moutinho, *et al.*, "Alternative procedure for the fabrication of close-spaced sublimated CdTe solar cells," *Journal of Vacuum Science and Technology A: Vacuum, Surfaces and Films,* vol. 18, pp. 1599-1603, 2000.
[30] H. R. Moutinho, *et al.*, "Electron backscatter diffraction of CdTe thin films: Effects of CdCl2 treatment," *Journal of Vacuum Science and Technology A: Vacuum, Surfaces and Films,* vol. 26, pp. 1068-1073, 2008.
[31] M. D. G. Potter, *et al.*, "Effect of interdiffusion and impurities on thin film CdTe/CdS photovoltaic junctions," *Journal of Materials Science: Materials in Electronics,* vol. 11, pp. 525-530, 2000.
[32] M. D. G. Potter, *et al.*, "Study of the effects of varying cadmium chloride treatment on the luminescent properties of CdTe/CdS thin film solar cells," *Thin Solid Films,* vol. 361, pp. 248-252, 2000.
[33] R. A. Enzenroth, *et al.*, "Correlation of stability to varied CdCl2 treatment and related defects in CdS/CdTe PV devices as measured by thermal admittance spectroscopy," *Journal of Physics and Chemistry of Solids,* vol. 66, pp. 1883-1886, 2005.
[34] A. Romeo, *et al.*, "COMPARISON OF CSS-CdTe AND PVD-CdTe WITH DIFFERENT ACTIVATION PROCESSES," in *22nd European Photovoltaics Solar Energy Conference,* Milan, Italy, 2007.
[35] S. A. Galloway, *et al.*, "Study of the effects of post-deposition treatments on CdS/CdTe thin film solar cells using high resolution optical beam induced current," *Applied Physics Letters,* vol. 68, pp. 3725-3725, 1996.
[36] H. R. Moutinho, *et al.*, "Studies of recrystallization of CdTe thin films after CdCl2 treatment," in *Proceedings of the 1997 IEEE 26th Photovoltaic Specialists*

Conference, September 29, 1997 - October 3, 1997, Anaheim, CA, USA, 1997, pp. 431-434.
[37] H. R. Moutinho, *et al.*, "Effects of CdCl2 treatment on the recrystallization and electro-optical properties of CdTe thin films," *Journal of Vacuum Science and Technology A: Vacuum, Surfaces and Films*, vol. 16, pp. 1251-1257, 1998.
[38] W. K. Metzger, *et al.*, "Time-resolved photoluminescence studies of CdTe solar cells," *Journal of Applied Physics*, vol. 94, pp. 3549-3555, 2003.
[39] B. E. McCandless and R. W. Birkmire, "Analysis of post deposition processing for CdTe/CdS thin film solar cells," *Solar Cells*, vol. 31, pp. 527-535, 1991.
[40] H. R. Moutinho, *et al.*, "Investigation of polycrystalline CdTe thin films deposited by physical vapor deposition, close-spaced sublimation, and sputtering," *Journal of Vacuum Science & Technology A: Vacuum, Surfaces, and Films*, vol. 13, pp. 2877-2877, 1995.
[41] Y. Qu, *et al.*, "HCl vapor post-deposition heat treatment of CdTe/CdS films," in *Photovoltaic Specialists Conference, 1996., Conference Record of the Twenty Fifth IEEE*, 1996, pp. 1013-1016.
[42] T. X. Zhou, *et al.*, "Vapor chloride treatment of polycrystalline CdTe/CdS films," in *Photovoltaic Energy Conversion, 1994., Conference Record of the Twenty Fourth. IEEE Photovoltaic Specialists Conference - 1994, 1994 IEEE First World Conference on*, 1994, pp. 103-106 vol.1.
[43] T. Potlog, *et al.*, "Influence of annealing in different chlorides on the photovoltaic parameters of CdS/CdTe solar cells," *Solar Energy Materials and Solar Cells*, vol. 80, pp. 327-334, 2003.
[44] P. D. Paulson and V. Dutta, "Study of in situ CdCl2 treatment on CSS deposited CdTe films and CdS/CdTe solar cells," *Thin Solid Films*, vol. 370, pp. 299-306, 2000.
[45] N. Nakayama, *et al.*, "Ceramic Thin Film CdTe Solar Cell," *Japanese Journal of Applied Physics*, vol. 15, p. 2281.
[46] H. R. Moutinho, *et al.*, "Effects of CdCl2 treatment on the recrystallization and electro-optical properties of CdTe thin films," *Journal of Vacuum Science and Technology A: Vacuum, Surfaces and Films*, vol. 16, pp. 1251-1257, 1998.
[47] B. E. McCandless, *et al.*, "Optimization of vapor post-deposition processing for evaporated CdS/CdTe solar cells," *Progress in Photovoltaics: Research and Applications*, vol. 7, pp. 21-30, 1999.
[48] J. F. Hiltner and J. R. Sites, "Micron-resolution photocurrent of CdTe solar cells using multiple wavelengths," in *II - VI Compound Semiconductor Photovoltaic Materials, April 16, 2001 - April 20, 2001*, San Francisco, CA, United states, 2001, pp. H981-H986.
[49] D. Bonnet and P. Meyers, "Cadmium-telluride - material for thin film solar cells," *Journal of Materials Research*, vol. 13, pp. 2740-2753, 1998.
[50] ICDD, "JCPDS-ICDD Card No. 15-0770," ed. Newton Square, PA.
[51] C. Suryanarayana and M. G. Norton, *X-Ray diffraction a practical approach*. New York: Plenum Press, 1998.
[52] C. S. Ferekides, *et al.*, "High efficiency CSS CdTe solar cells," *Thin Solid Films*, vol. 361, pp. 520-526, 2000.

[53] A. L. Fahrenbruch and R. H.-. Bube, *Fundamentals of solar cells photovoltaic solar energy conversion*. New York: Academic Press, 1983.
[54] V. V. Plotnikov, *et al.*, "Dependence CdS/CdTe solar cells efficiency and nonuniformity on CdS layer thickness," in *Photovoltaic Specialists Conference, 2008. PVSC '08. 33rd IEEE*, 2008, pp. 1-2.
[55] J. R. Sites and T. J. Nagle, "LBIC analysis of thin-film polycrystalline solar cells," in *31st IEEE Photovoltaic Specialists Conference - 2005, January 3, 2005 - January 7, 2005*, Lake Buena Vista, FL, United states, 2005, pp. 199-204.
[56] M. Burgelman, *et al.*, "Modeling thin-film PV devices," *Progress in Photovoltaics: Research and Applications*, vol. 12, pp. 143-153, 2004.
[57] S. Fonash, "AMPS-1D (Analysis of Microelectronic and Photonic Structures)," BETA 1.00 ed: Pennsylvania State University and Electric Power Research Institute, 1997.
[58] M. Burgelman, "SCAPS," 2.9.02 ed: March Burgelman, Electronics and Information Systems, University of Gent, 2010.
[59] S. Fonash, "A Manual for AMPS 1-D," ed: Pennsylvania State University and Electric Power Research Institute, 1997.
[60] M. Gloeckler, *et al.*, "Numerical modeling of CIGS and CdTe solar cells: Setting the baseline," in *Proceddings of the 3rd World Conference on Photovoltaic Energy Conversion, May 11, 2003 - May 18, 2003*, Osaka, Japan, 2003, pp. 491-494.
[61] K. Ohata, *et al.*, "Optical Energy Gap of the Mixed Crystal CdSxTe1-x," *Japanese Journal of Applied Physics*, vol. 12, p. 1641, 1973.

APPENDIX A: Baseline Modeling Properties

General Device Properties			
	Front	**Back**	
barrier height, Φb (eV)	EC-EF = Φbn = 0.1	EF-EV = Φbp = 0.4	
electron surface recombination velocity, Se (cm/s)	1.00E+07	1.00E+07	
hole surface recombination velocity, Sh (cm/s)	1.00E+07	1.00E+07	
reflectivity, Rf (1)	0.1	0.8	
Layer Properties			
	SnO_2	**CdS**	**CdTe**
layer width, W (nm)	500	200	1500
relative permittivity, $\varepsilon/\varepsilon_0$ (1)	9	10	9.4
electron mobility, μ_e (cm^2/Vs)	100	100	320
hole mobility, μ_h (cm^2/Vs)	25	25	40
electron desity, n (cm^{-3})	1.00E+17	1.00E+17	-
hole density, p (cm^{-3})	-	-	1.00E+15
band gap, E_g (eV)	3.6	2.4	1.5
effective density of states in the conduction band, N_C (cm^{-3})	2.20E+18	2.20E+18	8.00E+17
effective density of states in the valence band, N_V (cm^{-3})	1.80E+19	1.80E+19	1.80E+19
conduction band offset, ΔE_C (eV)	0	0 to -0.1	-0.1
Gaussian (midgap) Defect States			
	SnO_2	**CdS**	**CdTe**
donor-like defect density, N_{DG} (cm^{-3})	1.00E+15	-	2.00E+14
acceptor-like defect density, N_{AG} (cm^{-3})	-	1.00E+18	-
donor peak energy in, E_D (eV)	midgap	midgap	midgap
acceptor peak energy in, E_A (eV)	midgap	midgap	midgap
distribution width, W_G (eV)	0.1	0.1	0.1
electron capture cross-section, σ_e (cm^2)	1.00E-12	1.00E-17	1.00E-12
hole capture cross-section, σ_h (cm^2)	1.00E-15	1.00E-12	1.00E-15

Source: Gloeckler et al [60]